To my uncle Tonino

# Acknowledgements

I would like to acknowledge Prof.Amedeo Capozzoli to have given to me the possibility to spend six months at DLR in Oberpfaffenhofen for doing my Master Thesis.

I thank Angelo Liseno and my collegues at DLR, Matteo Nannini, Rolf Scheiber and Andreas Reigber for advices, encouragemets and the entire supervision of the work.

I thank all my collegues at DLR for support, scientific interaction and for all the free-time enjoyed with them.

My family for backing me up.
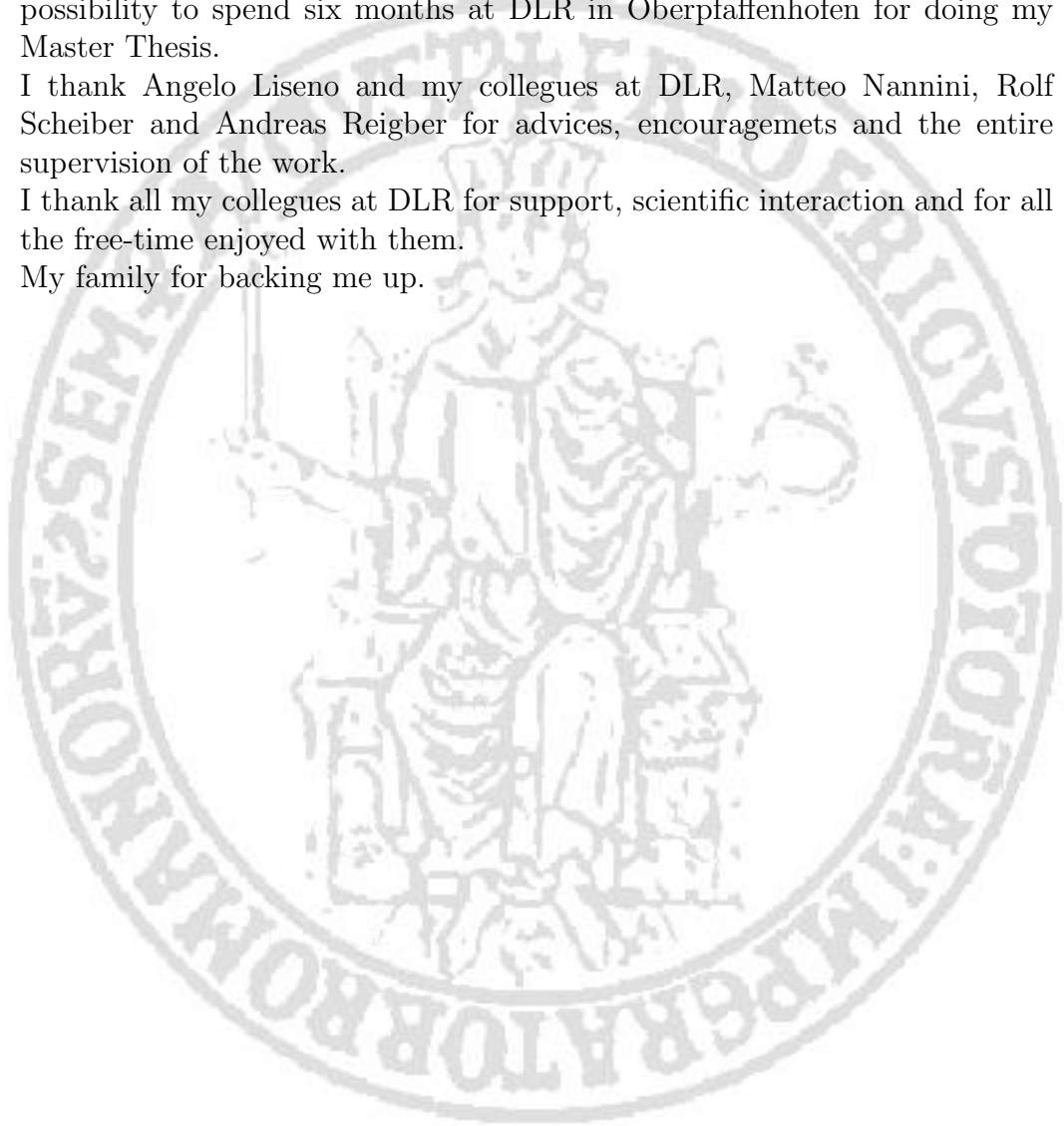
Introduction

In the last decades large scale Earth's monitoring has become possible thanks to the radar instruments. These systems are useful to monitor a scene and collect measurements even if we are far from it. In particular they have increased the applicability of *remote sensing* techniques, extending it to the vegetated areas monitoring. These imaging radars are airborne or spaceborne radars which generate a reflectivity map of an illuminated area through trasmission and reception of electromagnetic energy. Special attention has been paid to synthetic aperture radar (SAR) because of its high spatial resolution and multivarious information content. SAR sensors operate in the microwave region of the elctromagnetic spectrum with wavelengths between 1cm and several meters. As an active system, a SAR emits by itself microwave radiation to the ground and measures the electromagnetic backscattered field. The measurements are then processed to obtain a high resolution image. Because SAR systems operate with an illumination of their own, they can perform equally well during day and night. A SAR system consists of a transmitter and a receiver; if they are different the radar system is known as *bi-static* or *multi-static* (depending on the number of the receivers), otherwise if they coincide, it will be called *monostatic*.

One limitation of a SAR system is due to the cylindrical simmetry of the acquisition that does not allow to evaluate the height of an observed point. Two main extensions of conventional SAR have been pursued in the past to resolve the limitation in the elevation: SAR *interferometry* and SAR *polarimetry*. SAR interferometry tries to break the cylindrical symmetry using two acquisitions obtained along two parallel paths separeted by a baseline B. The drawback of this method is that it is not able to resolve several scatterers in the same resolution cell. SAR polarimetry is another major extension of conventional single channel SAR imaging. The main feature is that it allows a discrimination of different types of scattering mechanisms. Polarimetric SAR interferometry (POLInSAR) is a new technique that tries to combine the capability of interferometry to extract the height information with the polarimetric capability to decompose the backscattered signal in a sum of

different scattering mechanisms. With POLInSAR the topographic height of the phase centre of each extracted scattering mechanism can be estimated independently. Anyway this technique fails when we want to resolve two scatterers at different height with the same scattering mechanism.

This drawback gives birth to an onther type of SAR systems called SAR Tomography (SARTom). A first demonstration of SARTom for the airborne case was done in 1998. Through the several acquisitions it is possible to build up an aperture in the direction perpendicular to the flight path allowing to define a vertical resolution. This capability allows a 3-dimensional (3D) imaging of an observed scene. In order to achieve good resolution a big number of tracks is required. Moreover, the maximum volume height defines the sampling along the tomographic aperture that must respect the Nyquist criterion to avoid aliasing. SARTom offered for the first time the possibility to see through the vegetation. This feature is very important in the scenario of Kyoto protocol. In the last years, in fact, the need to monitor forests has increased in order to extract information about their height and for forestry classification. In particular, the height of forest has become the key parameter to do an analysis of the global carbon stocks. In this context, the thesis deals with a new approach to reduce the number of tracks, to present a strategy to design a constellation for SAR Tomography and to investigate on an inversion parametric approach to retrieve the reconstruction in the height direction in order to evaluate the ground and mean canopy height. One possibility to retrieve information about the height consists in solving a linear inverse problem with SVD. Concerning the design of the transmitting-receiving scheme, the choice of the number and the locations of the spatial acquisitions is of fundamental importance in order to retrieve the 3D structure. Formally, as long as a linear scattering model of the scenario is employed and the available a priori knowledge is exploited, the reconstruction by a SVD approach should follow a first design stage of the measurements to be performed having the aim of improving the ill-conditioning. This can be performed by optimizing the behaviour of the singular values as a function of the parameters defining the acquisition scheme. Concerning the inversion of the problem to obtain a reconstruction, an algorithm based on a global minimization of a funtional is presented in the second part of the work. This approach could lead to a better resolution of the reconstruction.

In Chapter 1 we introduce the principles of SAR data processing. SAR interferometry is also introduced as first step to overcome limitation of conventional SAR. A brief look at Polarimetry and Polarimetric SAR interferometry is done in order to point out the reason of using SAR Tomography. An application of SARTom is presented in the framework of forest biomass

estimation.

In Chapter 2 we formulate the problem and present the main approach for the focusing of a tomographic signal. The Fourier based Specan is presented showing its need to use a large number of tracks. Spectral estimation methods,CAPON and MUSIC, are presented.

Chapter 3 relates to the main work of the thesis. In the first part we present the inversion based on Singular Value Decomposition in order to reconstruct the density profile in the height direction. Then, we use SVD to optimise the constellation with the reduced number of tracks. The second part involves a different apporach to the problem. We implement a parametric algorithm for inversion based on the minimization of a functional. We present a global iterative stochastic algorithm for optimisation known as Multi-Level Single Linkage method.

In Chapter 4 we presents results obtained with SVD inversion and the parametric inversion using simulated data. Then we present the data set for the experimental data; the data set is property of DLR. It has been acquired from E-SAR over the forest of Dornstetten (Germany) in September 2006. We show the result ontained with SVD inversion using the real data. Finally, we combine the SVD optimisation of the constellation with the parametric inversione in the case of real data and reduced constellation. Conclusions and outlook are carried out at the end of the chapter.

Contents

List of Figures

List of Symbols and Acronyms

α_{ra}	angular resolution of antenna
B	interferometric baseline
c	speed of light
Γ	Gamma function
d	tomographic baseline
δ_{az}	azimuth resolution
δ_{sr}	slant-range resolution
Δt	time delay
h_f	forest height
H	maximum volume height
H_{pol}	polarimetry scattering entropy
L	antenna aperture length in azimuth
L_{sa}	synthetic aperture length
λ	radar wavelength
N	number of SAR images
N_b	number of basis functions
Φ	interferometric phase
$p(t)$	pulse envelope
r	sensor-to-target range
r_o	sensor-to-target range at closest approach
ρ	reflectivity function
$[S]$	scattering matrix
s	SAR signal
s_t	transmitted signal
s_r	received signal
T_r	pulse width
v	sensor velocity
W	signal bandwidth

DEM	Digital Elevation Model (above mean sea level)
DLR	German Aerospace Center
E-SAR	Experimental SAR of DLR
FT	Fourier Transform
GA	Genetic Algorithm
HH	horizontally received, horizontally transmitted
HV	horizontally received, vertically transmitted
InSAR	SAR interferometry
LOS	Line-of-Sight
MLSL	Multi Level Single Linkage
POLInSAR	Polarimetric SAR Interferometry
PRF	Pulse Repetition Frequency
PSLR	Peak-Sidelobe-Ratio
RCM	Range-Cell Migration
RVOG	Random Volume Over Ground
SA	Simulated Annealing
SAR	Synthetic Aperture Radar
SARTom	Synthetic Aperture Radar Tomography
SNR	Signal-to-Noise Ratio
SpecAn	Spectral Analysis
SVD	Singular Value Decomposition
VH	vertically received, horizontally transmitted
VV	vertically received, vertically transmitted

Chapter 1

Introduction on SAR Tomography

1.1 Synthetic Aperture Radar

Synthetic **A**perture **R**adar (**SAR**) refers to a particular set of active microwave sensors used to generate a two-dimensional reflectvity map of an examined scene. A common configuration of a SAR consists in mounting a microwave transmitter and receiver on a moving platform like an air-plane (Airborne SAR) or satellite (Spaceborne SAR); The SAR system illuminates an area on the ground by trasmitting electromagnetic pulses with a certain **P**ulse **R**epetition **F**requency (PRF) and receives the backscattered echoes, which are sampled and stored in a matrix, commonly called the raw data. Then the raw data are processed to obtain the reflectivity map of the scene. A SAR system can operate in different acquisition modes ([Cumm 04]):

- **Stripmap SAR**: In this mode, the antenna pointing direction is held constant as the radar platform moves;

- **Spotlight SAR**: This mode steers the antenna during the acquisition to illuminate the same area (*spot*);

- **ScanSAR**: In this mode the antenna beam is periodically changed to illuminate different subswath in the range direction.
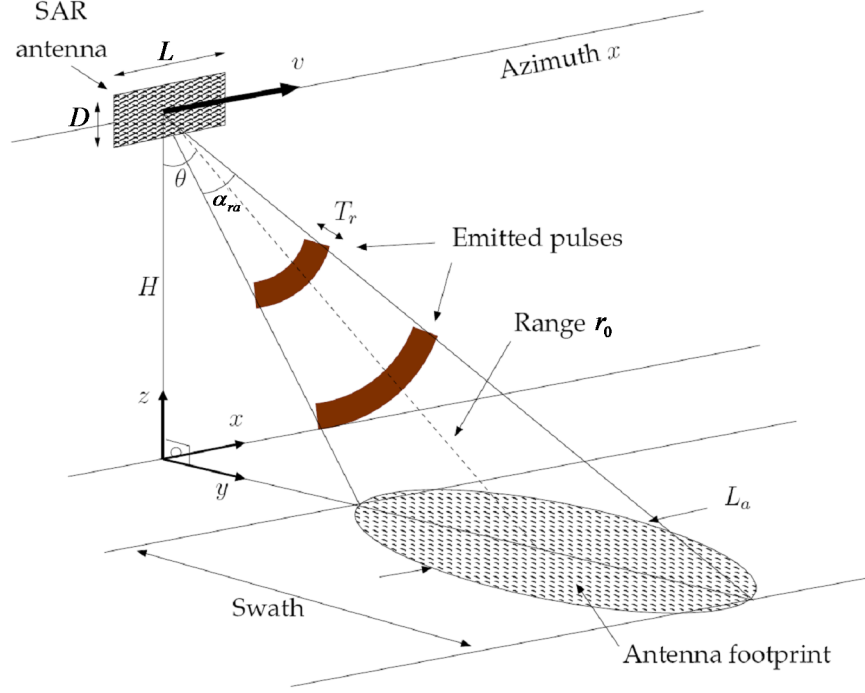
Figure 1.1: Airborne SAR stripmap geometry

In this work we focus on Airborne SAR systems and all the data presented have been acquired in the stripmap mode. In this case the antenna is oriented parallel to the flight direction (**azimuth**) and it looks sidewards to the ground (see Fig.1.1). The look direction of the antenna is normally called '**range**'or '**slant-range**'. The transmitter emits short radar pulses to the ground and after a certain time delay Δt the receiver will have the backscattered echoes from the ground. The time delay will be

$$\Delta t = \frac{2r}{c} \quad, \tag{1.1}$$

where c is the speed of light. With regard to the range spatial resolution, we can observe that two objects Δr-away can be effectively discriminated only if the received pulses - of width T_r - are completely separeted only. This condition implies that

$$\Delta r \geq \delta_{sr} = \frac{cT_r}{2} \quad, \tag{1.2}$$

where δ_{sr} is the achievable slant range resolution, which can be also expressed as function of the corresponding pulse bandwith W

$$\delta_{sr} = \frac{c}{2W} \quad. \tag{1.3}$$

2

Equation (1.3) suggests that it is possible to achieve high resolution in range only by using a very short pulse duration. The resulting energy densities are often difficult to handle in practice. To overcome this problem, a modern radar sytem, including a SAR one, transmits long linear frequency modulated pulses (chirp). In the along-track or azimuth direction, the resolution of a side-looking radar is obtained through the physical dimension of its aperture. It corresponds to the size of the antenna footprint on the ground along the flight direction. The angular resolution α_{ra} of an antenna of length L in the azimuth direction corresponds to the antenna beam width. For a wavelength λ it is given by

$$\alpha_{ra} = \frac{\lambda}{L} \qquad \Rightarrow \qquad \delta_{az} = \alpha_{ra}r_0 = \frac{\lambda r_0}{L} \quad , \qquad (1.4)$$

where δ_{az} is the spatial resolution in azimuth at a given range r_0. To achieve an high resolution in azimuth[1] we need to increase antenna dimension - that is not an easy task to be accomplished - and or to use short object distances. A SAR overcomes these problems taking advantage of the "phase history" of scatterers. The coherent sum of all the echoes received leads to the formation of a synthetic antenna. The situation is similar to that of an object imaged by a linear antenna, of length equal to the distance covered during the azimuth illumination time, when the antenna is far away from the object. In the case of a synthetic aperture only one antenna is used and thanks to the movement of the platform the different antenna positions are obtained. Considering that the phase difference between elements of the synthetic aperture results from a two-way path difference, the angular resolution of a synthetic aperture of length L_{sa} is:

$$\alpha_{sa} = \frac{\lambda}{2L_{sa}} \quad . \qquad (1.5)$$

The maximum length for the synthetic aperture corresponds to the length of the flight path from which a scatterer is illuminated or, likewise, to the size of the antenna footprint on the ground at the distance r_0,

$$L_{sa} = \alpha_{sa}r_0 = \frac{\lambda r_0}{L} \qquad \Rightarrow \qquad \delta_{az} = \alpha_{sa}r_0 = \frac{L}{2} \quad . \qquad (1.6)$$

According to equation (1.6) we can conclude that the achieved resolution is independent of the range distance and is determined only by the size of the real antenna. Typically an Airborne SAR has a resolution approximately up to 30cm.

---

[1] A Spaceborne system with an orbital height of 800Km and an antenna aperture of 15m shows a resolution of approximately 3Km only.

1.1.1 SAR data processing

The aim of SAR data processing is to obtain the best possible representation of a scene from the collected raw data. For a description of the scattering processes on the ground, a reflectivity function $\rho(x, r)$ can be used, which models the ground as a superposition of separeted δ-like point scatterers:

$$\rho(x, r) = \sum_n \rho_n \delta(x - x_n, r - r_n) \quad , \tag{1.7}$$

where ρ_n is the complex backscattering amplitude of the n-th scatterer and $\delta(x, r)$ the two dimensional DIRAC's delta-function. The transmitted pulses of the sensor at position x can be expressed as

$$s_t(x, t) = p(t) e^{jwt} \quad , \tag{1.8}$$

where $p(t)$ denotes a pulse envelope and w is the carrier frequency of the radar. Assuming that the system transmits and receives the same pulse at the same position (*stop and go approximation*), the echo of a scatterer positioned at (x_n, r_n) is received by the sensor after a time delay of

$$\Delta t_n(x, x_n, r_n) = \frac{2r(x - x_n, r_n)}{c} \quad . \tag{1.9}$$

The entire received echo at position x is a coherent superposition of all the echoes from the scatterers in the scene illuminated from that position[2]:

$$s_r^{tot}(x, t) = \sum_n \rho_n \delta \left(t - \frac{2r(x - x_n, r_n)}{c} \right) e^{-2jwr(x-x_n, r_n)/c} e^{jwt} \tag{1.10}$$

$$s_r^{tot}(x, t) = e^{jwt} \iint \rho(x_n, r_n) e^{-2jwr(x-x_n, r_n)/c} \delta(t - \Delta t_n) dx_n dr_n \quad . \tag{1.11}$$

We can notice that the echo phase of a scatterer depends on the trend of Δt_n and therefore on $r(x - x_n, r_n)$. As the sensor is positioned at $r = 0$, the range history of the n-th scatterer can be written as

$$r(x - x_n, r_n) = \sqrt{r_n^2 + (x - x_n)^2} \simeq r_n + \frac{(x - x_n)^2}{2r_n} \quad . \tag{1.12}$$

The echoes of this scatterer received from different azimuth positions x do not appear in the same range line, but on a hyperbolic curve centered at x_n

---

[2]In the receiver hardware the carrier frequency is removed by a quadratic demodulation before data recording.

and with a curvature dependent on r_n. This effect is referred in the literature as '*range cell migration*' ([Cumm 04],[Olm 93]). Because of this, range times and range distances are not interchangeable. In case that a short illumination path with respect to the distance to the object ($L_{sa} \ll r_n$) can be assumed, a parabolic approximation as in (1.12) is possible. This is the case for SAR sensors with moderate to low resolution. Under this approximation the total response of a single scatterer at position (x_n, r_n) sounds like:

$$s_r^n(x, x_n, r_n) = \rho_n e^{2jwr_n/c} \, e^{jw(x-x_n)^2/cr_n} \, rect\left(\frac{(x-x_n)}{L_{sa}}\right) \quad . \tag{1.13}$$

The intention of SAR processing is to focus the received energy of a scatterer on the position of the scatterer from which it originated. In practice, the task of this algorithm is to obtain an estimation of the original reflectivity function $\rho(x, r)$. The most common method is based on the concept of matched filtering. The image result $v(x, r)$ is obtained by correlating the raw data, pixel by pixel, with two-dimensional reference functions $h_{ref}(x, t, x_n, r_n)$. For one single pixel (x_n, r_n), this can be written as:

$$v(x_n, r_n) = \iint s_r^{tot}(x, t) h_{ref}(x, t, x_n, r_n) dx dt \quad . \tag{1.14}$$

An azimuth line of the image result can be obtained by:

$$v(x_n, r_n) = s_r^{tot}(x, t = 2r_n/c) \odot_x h_{ref}(x, r_n) \quad , \tag{1.15}$$

where $\odot_x$ denotes the correlation in the x-direction and $h_{ref}(x, r_n)$ is the matched reference function for focusing a point scatterer located in the range distance r_n. Because of the large amount of data acquired in modern high resolution radar systems, this time domain formulation is very slow and inefficient. Using the so-called '*Convolution Theorem*' the correlation can be expressed as a multiplication with a space inverted response in the wavenumber domain,

$$\tilde{V}(k_x, r_n) = \tilde{S}_r^{tot}(k_x, 2r_n/c) \tilde{H}_{ref}(k_x, r_n) \quad , \tag{1.16}$$

where $\tilde{V}(k_x, r_n)$, $\tilde{S}_r^{tot}(k_x, 2r_n/c)$ and $\tilde{H}_{ref}(k_x, r_n)$ are the FOURIER-transforms of $v(x_n, r_n)$, $s_r^{tot}(x, t = 2r_n/c)$ and $h_{ref}(x, r_n)$ in the x-dimension, respectively, and k_x denotes the spatial frequency in the azimuth direction. The transfer function $\tilde{H}_{ref}(k_x, r_n)$ can be obtained from $h_{ref}(x, r_n)$ by:

$$\tilde{H}_{ref}(k_x, r_n) = \frac{1}{2\pi} \int h_{ref}(x, r_n) e^{-jk_x x} dx \quad . \tag{1.17}$$

An approximation of the integral in (1.17) can be found by the stationary phase assumption [Olm 93]. With the stationary points found, the integral can be approximated as:

$$\tilde{H}_{ref}(k_x, r_n) = \frac{1}{2\pi} e^{\frac{jcr_n k_x^2}{4w}} \quad . \tag{1.18}$$

Going back to the time domain we obtain the azimuth line of the image result:

$$v(x_n, r_n) = L_{sa}\rho_n e^{\frac{2jwr_n}{c}} e^{\frac{jw}{cr_n}(x-x_n)^2} sinc\left(\frac{wL_{sa}}{cr_n}(x-x_n)\right) \quad , \tag{1.19}$$

where 'sinc'stands for the 'sinus cardinalis'-function $sin(x)/x$. As we can see

(a) (b)
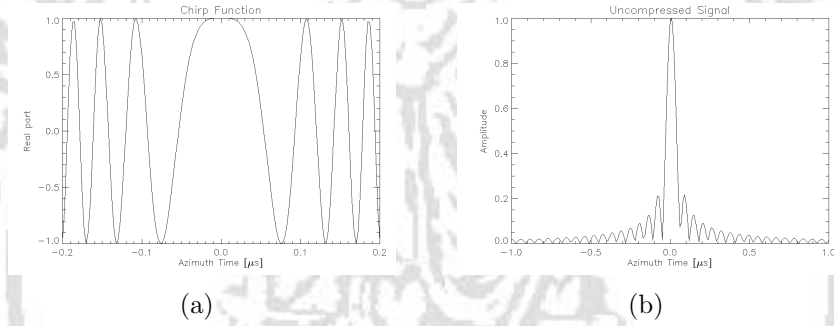
Figure 1.2: Signal Compression. (a) Chirp Signal, (b) Uncompressed signal

in (1.2) the first sidelobes are -13dB lower than the main peak. This can cause problems if a strong target is near to some weaker targets. Therefore, using an HAMMING-window function to weight the reference function it is possible to show a better Peak-Sidelobe-Ratio (PSLR).

(a) (b)
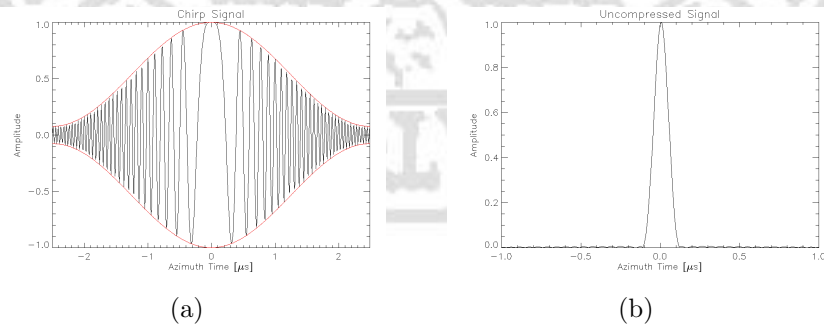
Figure 1.3: Signal Compression with Hamming windowing. (a) Chirp Signal, (b) Uncompressed signal

The PSLR of the compressed signal shown in 1.4 is now much better and has a value of averagely -43dB. To obtain the final two-dimensional point target response, we have to use a second reference function in the range direction. The final result is shown in the following picture. The input is the complex signal, as recorded by the SAR sensor. After an one dimensional FOURIER-transform in range direction, each range line is multiplied with the FOURIER-transform of the reference function in range. After the inverse FFT back to time domain, the data are compressed in range, but are still defocused in azimuth. Then a FOURIER-transform in azimuth is performed, followed by a multiplication of the FOURIER-transform of the reference function in azimuth. After the back-transformation, the complex image result is derived. When our scene is a real one with more than one scatterer there is

(a)   (b)   (c)
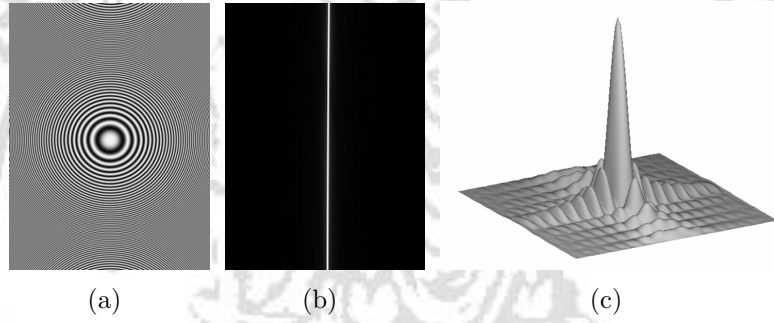
Figure 1.4: (a) Raw data, (b) Range uncompressed Raw data, (c) Poin target response

a high probability to incur in a degrading effect called '*speckle*' (see Figure 1.5). We know that the backscatter of each resolution cell or pixel is the combined effect of all the individual objects within the cell that return or scatter the radar signal. For this reason, cells that are adjacent to each other and appear visually very similar may have completely different backscatterer at radar wavelenghts. This is because the individual objects within the cell are positioned differently giving a different resultant backscatter. The variation in backscatter for otherwise homogeneous cells is the origin of the speckle and gives a graphy appearance to radar images. Speckle can be reduced through an averaging process in order to obtain a better estimation of the desired information. This process is known as '*multilook*'. The drawback is, of course, the resolution loss due to the averaging. The multilook process in frequency domain consists in dividing the spectrum, in separate looks, to later incoherently add the resulting images. The method for SAR processing presented in this subsection is a simplified algorithm using some approximations but is quite usable for SAR sensors with relatively low resolution. More advanced
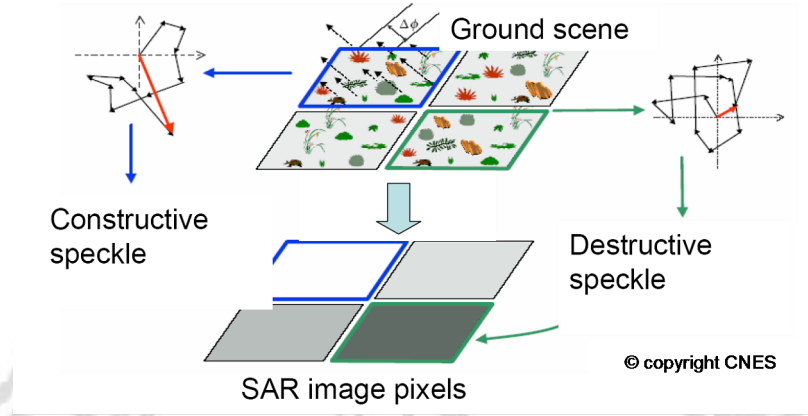
Figure 1.5: Speckle generation

algorithms, including range migration, become important for high resolution imaging and can be found in the literature ([Cumm 04]).

1.1.2 SAR terrain induced distortion

A quick glance comparing a radar image with an aerial photography or a satellite one will reveal obviuos differences caused by the fact that relief displacement is in the opposite directions. On aerial photographs relief displacement falls away from the nadir point because the top is imaged further from nadir than the base of a structure. In radar images the top of a structure may be imaged before the base. Thus, the relief displacement falls towards the nadir. Due to the side looking geometry, the relief displacement will be greater in slant range than ground range. The slant range distorsion occurs because the radar measures the distance to features in slant-range rather than true horizontal distance along the ground. This results in a varying image scale, moving from near to far range. The following subsections present typical terrain distorsion occurring in a radar image. The three characteristic distorsion resulting from the geometric relationship between the sensor and the terrain that are present in a radar image are ***foreshortening, layover and shadowing***. Foreshortening is the effect by which the foreslopes of hills and mountains appear to be compressed. As we can see in Figure 1.6, the simplified terrain element (hill) represented by the triangle ABC is illuminated by the radar beam and the echoes from points a, b and c are projected on the slant range image plane to points a', b' and c'. When $\overline{ab}$ is sloped towards the sensor S, but only so much that $\alpha < \gamma$, then the image
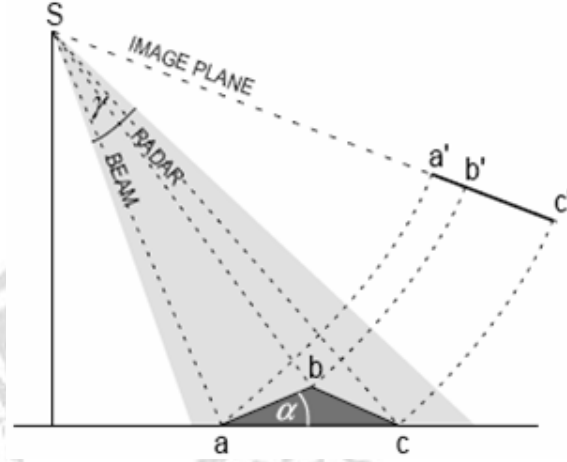
Figure 1.6: Foreshortening generation

$\overline{a'b'}$ will be shorter than $\overline{ab}$. When the slope is perpendicular to the beam, $\alpha = \gamma$, a' will coincide with b' so that all the energy scattered from the slope will be compressed into a single pixel. This is complete foreshortening and marks the transition to *layover*. Here $\alpha > \gamma$ and consequently b' precedes a'
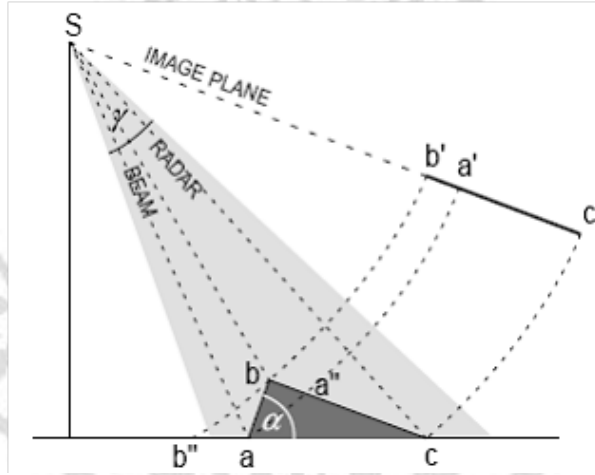
Figure 1.7: Layover generation

in range sequence. The echo from $\overline{ab}$ is distributed, but in reverse sequence and superimposed over that from $\overline{ba''}$. A third configuration is illustrated in Figure 1.7 where the back slope $\overline{bc}$ of the terrain is steep enough so that it cannot be illuminated by the radar beam. This occurs when the slope is and is known as *shadowing*. Backscatter information is lost, not only from area

9

Figure 1.8: Shadowing generation

$\overline{bc}$, but also from $\overline{cd}$ which is shadowed in the proper optical sense of the word. If we want to add further imaging capabilities to extract height information we need to use approaches different from SAR conventional processing.

1.2 SAR Interferometry

It has already been mentioned in the section 1.1 that the standard SAR imaging problem displays a cylindrical symmetry. This means that two scatterers can have the same range distance to the sensor but are seen under a different look angle. In this case the radar echo arrives at the same time at the sensor, and they cannot be solved. This condition implies that is not possible to obtain any information about the height. A first step to introduce some imaging capabilities in the vertical direction is to use cross-track interferometry.

1.2.1 Cross-Track Interferometry

The main goal of cross-track interferometry is to break cylindrical symmetry and to extract topographic information using two SAR images acquired from slightly different positions ([Cumm 04]). The two images can either be acquired by using two antennas on the same platform simultaneosly (**single-pass interferometry**), or by using one antenna in repeated passes over the

Figure 1.9: Sketch of SAR interferometry geometry

same area at different times (**repeat-pass interferometry**). The basic imaging geometry is shown in Figure 1.9. The scene is observed from two antennas S_1 and S_2, separeted by a baseline B with a slope ϵ. At a certain topographic height z a scatterer ρ is located, which is observed under the off-nadir angle θ. The range distances of two antennas to the scatterer are r_1 and r_2, respectively. The receiving signals s_1 and s_2, after SAR processing, consist of the complex terrain reflectivity $\rho(r)$ modulated by a phase term due to range distance to the scatterer:

$$s_1(r_1) = |\rho_1(r_1)|e^{j\angle\rho_1(r_1)} \quad and \quad s_2(r_2) = |\rho_2(r_2)|e^{j\angle\rho_2(r_2)} \quad . \qquad (1.20)$$

The phase of the received signals consists of two contributions: a deterministic one associated to the round trip path lenghts, and a random phase contribution due to the different terrain reflectivity charateristic:
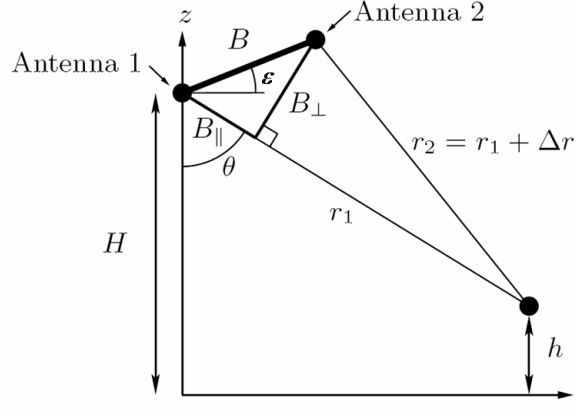
$$\angle s_1(r_1) = 2\frac{2\pi}{\lambda}r_1 \quad and \quad \angle s_2(r_2) = 2\frac{2\pi}{\lambda}r_2 \quad . \qquad (1.21)$$

The knowledge of the two antenna locations and of the corresponding range distances permits the determination of the location of the point P in the three-dimensional space by simple triangulation. The accuracy depends on the precision of estimation of these parameters. Before interferograms can be formed, the two images have to be precise and coregistrated to each other. Because they are acquired in repeat-pass mode the tracks are not syncronized, a certain offset in azimuth might occur. Because of the baseline, a similar thing happens in range direction. At this point a complex interferogram is formed just multiplying the first signal with the complex conjugate of the

second signal as

$$s_1(r_1)s_1^*(r_2) = |s_1 s_2^*|e^{-j\frac{4\pi}{\lambda}\Delta r_{12}} \quad . \tag{1.22}$$

Thus, the phase of the interferogram corresponds to the path difference of the two signals Δr_{12}:

$$\Phi = -\frac{4\pi}{\lambda}\Delta r_{12} + 2\pi N \quad, \qquad where \quad N \in \mathbb{Z} \quad . \tag{1.23}$$

Using equation (1.23), it is possible to measure the range difference Δr_{12} in terms of the interferometric phase. Using the Carnot Theorem, Δr_{12} may be expressed in terms of imaging geometry parameters as

$$r_2^2 = r_1^2 + B^2 + 2r_1 B \sin(\theta - \epsilon) \quad \Rightarrow \quad \sin(\theta - \epsilon) = \frac{r_2^2 - r_1^2 - B^2}{2r_1 B} \quad, \tag{1.24}$$

where ϵ denotes the slope of the baseline with respect to the horizontal plane, and θ the look-angle from the first antenna. With known θ, the height of the scatterer can be calculated by:

$$h = h_0 - r_1 \cos\theta \quad . \tag{1.25}$$

If the baseline B is small compared to the slant range distance we can use the parallel ray approximation; substituting $r_2 = r_1 + \Delta r_{12}$ in (1.24) and neglecting Δr_{12}^2, we have:

$$\Delta r_{12} = B \sin(\theta - \epsilon) + \frac{B^2}{2r_1} \quad \Rightarrow \quad \Delta r_{12} = B \sin(\theta - \epsilon) \quad . \tag{1.26}$$

Furthermore, it is common to decompose the baseline B into a parallel $B_\parallel$ and orthogonal $B_\perp$ to the line-of-sight of range direction component

$$B_\parallel = B \sin(\theta - \epsilon) \quad B_\perp = B \cos(\theta - \epsilon) \quad, \tag{1.27}$$

then the interferometric phase is:

$$\Phi = -\frac{4\pi}{\lambda}B \sin(\theta - \epsilon) = -\frac{4\pi}{\lambda}B_\parallel \quad . \tag{1.28}$$

Consider now the following two scenarios. In a first scenario, a second point P' located at the same height z of P, but at a different range distance $r_1 + \Delta r_{12}$, as shown in The look-angle will change about $\Delta\theta_R$, and the corresponding interferometric phase of P' is

$$\Phi' = -\frac{4\pi}{\lambda}B \sin(\theta + \Delta\theta_R - \epsilon) \quad . \tag{1.29}$$

The phase difference between the two points in the interferogram is given by

$$\Delta\Phi_R = \frac{4\pi}{\lambda}B[\sin{(\theta + \Delta\theta_R - \epsilon)} - \sin{(\theta - \epsilon)}] \approx -\frac{4\pi}{\lambda}B\sin{(\theta - \epsilon)}\Delta\theta_R \quad . \tag{1.30}$$

Applying a small angle approximation, $r_1\Delta\theta_R \approx r_1\sin\Delta\theta_R = \Delta r_{12}/\tan\theta$, the phase difference between the two points in the interferogram as a function of their range difference Δr_{12} becomes

$$\Delta\Phi_R = -\frac{4\pi}{\lambda}\frac{B\sin{(\theta - \epsilon)}\Delta r_{12}}{r_1\tan\theta} = -\frac{4\pi}{\lambda}\frac{B_\perp\Delta r_{12}}{r_1\tan\theta} \quad . \tag{1.31}$$

Equation (1.31) states that a flat surface without topography generates a linear interferometric phase known as flat-earth phase component. This linear term has to be subtracted in order to relate directly the interferometric phase to the topography. In a second scenario now, we consider the point P' to be located at the same range distance r_1 as P, but at different height $z + \Delta z$ as shown in The look-angle will alter by $\Delta\theta_z$, and the phase in the interferogram will be

$$\Phi' = -\frac{4\pi}{\lambda}B\sin{(\theta + \Delta\theta_z - \epsilon)} \quad . \tag{1.32}$$

According to the previous considerations, in order to obtain the excessive phase contribution caused by the height difference between the two points, we have to subtract the range dependent phase component

$$\Delta\Phi_z = -\frac{4\pi}{\lambda}B[\sin{(\theta + \Delta\theta_z - \epsilon)} - \sin{(\theta - \epsilon)}] \approx \frac{4\pi}{\lambda}B\sin{(\theta - \epsilon)}\Delta\theta_z \quad . \tag{1.33}$$

Finally, using again $r_1\Delta\theta_z \approx r_1\sin\Delta\theta_z = \Delta z/\sin\theta$, the interferometric phase difference related to the height variation Δz, results as

$$\Delta\Phi_z = -\frac{4\pi}{\lambda}\frac{B\sin{(\theta - \epsilon)}\Delta z}{r_1\sin\theta} = -\frac{4\pi}{\lambda}\frac{B_\perp\Delta z}{r_1\sin\theta} \quad . \tag{1.34}$$

As shown by Equation (1.34), the interferometric phase differences are directly related to the topographic height of the scene[3]. Up to now the fact that the interferometric phase is measured only modulo 2π has been ignored. Before applying equation (1.34), it is necessary to reconstruct the absolute phase from the measured '*wrapped*'phase. Several so called '*phase unwrapping*' algorithms have been addressed in recent publications ([Prat 04]). An

---

[3]For example, an airborne L-band system with a flight height of 4000m achieve a resolution of at least 50cm in height with a baseline of 25m.

important factor in SAR interferometry is the quality of the interferogram. In general, the assumption that the complex reflectivity is angle-independent is not correct. For repeat pass interferometry, a stability over time is additionally necessary. Therefore, the interferogram appears usually noisy, reducing the precision of the height estimation as well as limiting the ability to resolve the 2π ambiguities. A measure of the interferogram quality is the normalised complex cross-correlation between the two SAR images, known as the interferometric coherence:

$$\gamma := -\frac{|E(s_1 s_2^*)|}{\sqrt{E(s_1 s_1^*)E(s_2 s_2^*)}} \quad . \tag{1.35}$$

The coherence varies between 0 (no correlation) and 1 (the two images are identical). In figure 1.10 present a block diagram of a simple SAR Interferometry processing. Even if SAR interferometry introduce some capabilities
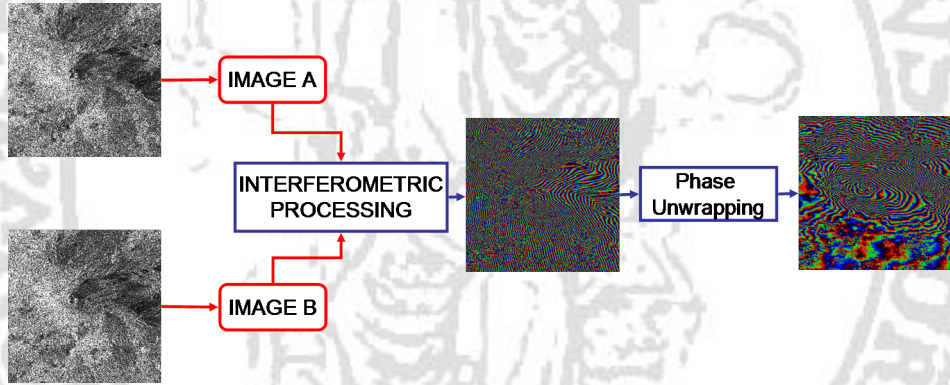
Figure 1.10: Block diagram to obrain an interferogram with two images using the Flat-Earth removal

to map a scene in the third dimension, it has several deficiencies. A major limitation of interferometry is its inability to resolve two or more scatterers located in the same range distance. SAR interferometry alone can only produce a surface and never a volumetric representation of the examined scene.

1.3 SAR Polarimetry

A first contribution to overcome the ambiguity problem in vertical direction of single-channel SAR remote sensing comes from polarised waves ([Clou 98]).

(a) Interferogram with flat term

(b) Interferogram without flat term

(c) Coherence map

Figure 1.11: Interferogram and coherence map

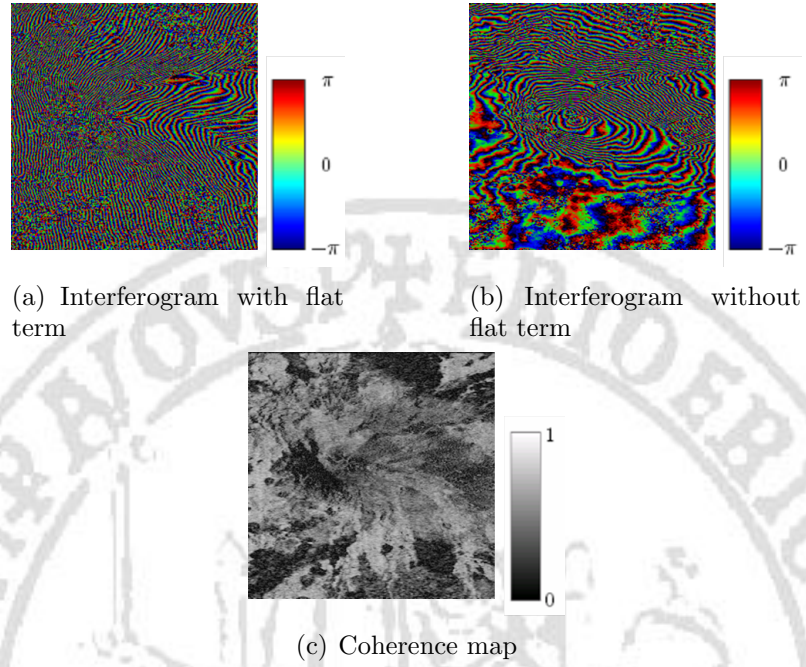A polarimetric SAR system is able to measure the backscattered electric field, including its polarisation state. The scattering mechanism leads to changes of the polarisation of the trasmitted wave. Therefore, the polarisation of the backscattered wave depends both on the scattering properties of the object and the polarisation of the trasmitted wave. In this way is possible to extract additional information about the scattering process and to separate multiple contributions occuring in the same resolution cell related to different scattering mechanisms. The polarisation of an electromagnetic wave describes the behaviour of the oscillating electric field vector $\vec{E}_{tot}$. Due to the transverse nature of electromagnetic waves, the electric field vector lies in the plane orthogonal to the propagation direction. Therefore, any possible polarisation state can be decomposed in a linear combination of two components which are both orthogonal to the propagation direction:

$$\vec{E}_{tot} = E_h\vec{h} + E_v\vec{v} \quad , \tag{1.36}$$

where E_h and E_v denote the projection of E_{tot} onto the versors $\vec{h}$ and $\vec{v}$, which form a reference orthogonal basis. The projections E_h and E_v are complex quantities and describe the polarisation state of far-field electromagnetic wave. The first tool to describe scatterers using polarymetry is the $2x2$ complex scattering matrix $[S]$, which describe the relation between

transmitted and received wave:

$$\begin{pmatrix} E_h^r \\ E_v^r \end{pmatrix} = \begin{bmatrix} S_{hh} & S_{hv} \\ S_{vh} & S_{vv} \end{bmatrix} \begin{pmatrix} E_h^t \\ E_v^t \end{pmatrix} \quad . \tag{1.37}$$

E_h^t and E_v^t denote the horizontally and vertically polarised components of the transmitted field, and E_h^r and E_v^r the ones of the measured backscattered field, respectively. The elements of $[S]$ denote the complex scattering amplitudes; S_{hh} and S_{vv} are referred to as the co-polar, S_{hv} and S_{vh} as the cross-polar components. In radar, the scattering matrix is measured by transmitting and receiving successive pulses in $h-$ and $v-$ polarisation. It has to be noted that in the case of backscattering in a reciprocal medium and symmetric scatterers, the two off-diagonal elements of $[S]$ are identical. The measuring of full polarimetric scattering matrix allows characterizing an object through its polarisation signature and to identify and separate different elementary scattering mechanisms. An alternative formulation of the

Figure 1.12: Polarimetric E-SAR image of Oberpfaffenhofen, incl. DLR (HH-green, VV-blue, HV,red).

polarimetric scattering problem uses a vectorial formulation. This approach replaces the scattering matrix by a three-dimensional scattering feature vector $\vec{k}_3$ by projecting the scattering matrix onto an orthonormal set of basis matrices of a three dimensional vector space:

$$[S] = \begin{bmatrix} S_{hh} & S_{hv} \\ S_{vh} & S_{vv} \end{bmatrix} \quad \Rightarrow \quad \vec{k}_3 = trace([S]\Upsilon) = [k_0, k_1, k_2]^T \quad , \tag{1.38}$$

where $trace([S]\Upsilon)$ is the sum of the diagonal elements of the matrix while Υ denotes a complete set of 2x2 complex basis matrices. Due to reciprocity, the

cross-polarized elements are identical, $S_{hv} = S_{vh}$, and the scattering vector is commonly given as a 3-element vector. The basis Υ is not unique and so there are more than one way for decomposing the same scattering matrix ([Reig 01]). In the literature one important basis set is formed by the three PAULI spin matrices:

$$\Upsilon_P = \sqrt{2} \left(\begin{bmatrix} 1 & 0 \\ 0 & 1 \end{bmatrix}, \begin{bmatrix} 1 & 0 \\ 0 & -1 \end{bmatrix}, \begin{bmatrix} 0 & 1 \\ 1 & 0 \end{bmatrix} \right) \quad , \tag{1.39}$$

while the corresponding scattering vector has the form:

$$\vec{k}_{3P} = \frac{1}{\sqrt{2}} \left[S_{hh} + S_{vv}, S_{hh} - S_{vv}, 2S_{hv} \right]^T \quad . \tag{1.40}$$

The PAULI vectorisation is very common because it can be physically interpreted in terms of three basic scattering mechanisms:

- PAULI 1 ($S_{hh} + S_{vv}$): emphasizes isotropic 'odd'-bounce scatterers, such as idealised 'flat'surfaces or trihedral corner reflectors;

- PAULI 2 ($S_{hh} - S_{vv}$): emphasizes isotropic 'even '-bounce scatterers, like for example a double bouce;

- PAULI 3 ($2S_{hv}$): corresponds to isotropic 'even'-bounce scattering with an orientation rotated by $\pi/4$ like a double bounce target whose axis is rotated to the line-of-sight direction (e.g. dihedral corner reflectors with a rotation of 45 degrees). Also in case of random volume scattering, a significant contribution of the backscattering is found in this third component ok $\vec{k}_{3P}$.

In general, it is possible to evaluate the contribution of a certain scattering mechanism $\vec{w}$ of the measured scattering vector $\vec{k}$ just calculating its projection:

$$\mu = \vec{w}^{\dagger} \cdot \vec{k} \quad , \tag{1.41}$$

where $\dagger$ denotes the adjoint operation[4] and μ is the complex scattering amplitude of the chosen scattering mechanism.

The scattering matrix is able to characterize only one single deterministic scatterer present in each resolution cell. This approach fails if we consider distributed scatterers. For this kind of targets the backscattering of each resolution cell is related to the coherent superposition of several scattering

---

[4]complex conjugate transpose

processes. Due to the presence of speckle noise, these scatterers can be described only in a statistical way. One possible approach is to introduce a coherency matrix $[T_3]$ and try to decompose it as the combination of different canonical scattering mechanisms in form of second order statistics, such as the variance and the correlation for all elements of $[S]$. In the PAULI-basis, the coherency matrix is given by

$$[T_3] = \langle \vec{k}_{3P} \vec{k}_{3P}^\dagger \rangle \quad,$$

with $\langle \ldots \rangle$ denoting a spatial averaging. One possibility to decompose $[T_3]$ was proposed by S.R. Cloude and is based on eigenvector analysis. Due to the spatial averaging $[T_3]$ is in general of full rank 3 and as consequence of its definition it is a hermitian positive semidefinite matrix. This means that it can be written as a sum of three indipendent coherency matrices:

$$[T_3] = \sum_{i=1}^{3} [T_3]_i = \lambda_1(\vec{u}_1\vec{u}_1^\dagger) + \lambda_2(\vec{u}_2\vec{u}_2^\dagger) + \lambda_3(\vec{u}_3\vec{u}_3^\dagger) \quad, \qquad (1.42)$$

where λ_i are the eigenvalues of $[T_3]$ and $\vec{u}_i$ their orthonormal eigenvectors. Eigenvalues represents also the amplitude of the scattering process described by the corresponding eigenvector. A way to evaluate if all three scattering mechanism are dominant or not is to define the polarimetric scattering entropy H_{pol}. It is defined as

$$H_{pol} := \sum_{i=1}^{3} -P_i \log_3 P_i \quad, \quad with \quad P_i = \frac{\lambda_i}{\sum_{j=1}^{3} \lambda_j} \quad. \qquad (1.43)$$

Entropy can assume a value between 0 and 1. An entropy of 0 means that thare is only one scattering mechanism dominant (or one significant eigenvalue). This condition is equivalent to have a deterministic scatterer described by a single scattering matrix. On the other hand, an entropy close to 1 occurs when eigenvalues are identical and there are several equally dominant scattering processes.

Summarizing, using polarimetry for target decomposition allows the separation of scatterers with different shapes and orientations occuring inside the same resolution cell. This means that polarimetry alone is not sufficient to extract information about the spatial height or vertical distribution of scatterers in our scene.

1.3.1 Polarimetric SAR Interferometry

Polarimetric **SAR In**terferometry (**POLInSAR**) is an approach to combine the features of polarimetry with the generation of an interferogram

([Clou 03]). In this way in the same resolution cell it is possible to evaluate the height of objects with different scattering mechanisms.

Using polarimetry implies that we have a scattering received vector for each polarisation. This means that the interferogram generated from two slightly different positions is a vectorial operation which gives a 6x6 coherency matrix:

$$\Lambda_{12} := \langle \vec{k}_1 \cdot \vec{k}_2^\dagger \rangle = \begin{bmatrix} T_{11} & \Omega_{12} \\ \Omega_{12}^\dagger & T_{22} \end{bmatrix} \quad , \tag{1.44}$$

where superscripts 1 and 2 refer to the measurements at the two positions of the baseline, T_{ii} is the 3x3 polarimetric coherency matrices and Ω_{ij} is the interferogram for a certain polarisation. Defining two scattering processes $\vec{w}_1$ and $\vec{w}_2$ the complex coherence will be:

$$\tilde{\gamma}(\vec{w}_1, \vec{w}_2) = \frac{\vec{w}_1^\dagger \Omega_{12} \vec{w}_2}{\sqrt{\vec{w}_1^\dagger T_{11} \vec{w}_1} \sqrt{\vec{w}_2^\dagger T_{22} \vec{w}_2}} \quad , \tag{1.45}$$

If there are two different scatterers separated in height it is now, in principe, possible to extract the height of both. One application, presented by Cloude ([Clou 03]), is based on a three-stage inversion process to determine the height of forests. A two-layer model, is one used for the ground response and the second one for the canopy. In this 2-layer case or **R**andom-**V**olume-**O**ver-**G**round (**RVOG**),([Clou 03], [Clou 98]), the observed coherence is given by the formula

$$\tilde{\gamma}(\vec{w}) = e^{j\phi}\frac{\tilde{\gamma}_v + \mu(\vec{w})}{1 + \mu(\vec{w})} = e^{j\phi}[\tilde{\gamma}_v + \frac{\tilde{\gamma}_v}{1 + \mu(\vec{w})}(1 - \tilde{\gamma}_v)] \quad , \tag{1.46}$$

Here the ground phase ϕ and complex volume coherence $\tilde{\gamma}_v$ are combined with the parameter μ, the ground-to-volume ratio that includes the effects of wave extinction in the medium. By isolating the polarisation dependent terms the resulting coherence lies along a straight line in the complex coherence plane. The line intersects the circle at two points. One of these is the underlying topography related phase; the other one is a false solution and must be rejected. The first stage is to find straight line inside the unit circle of interferometric coherence that best fits my data. To do this we vary two phase variable ψ_1 and ψ_2 as shown in Figure 1.13. The output from stage 1 is a set of ψ_1 and ψ_2 paired values for each pixel. The next stage involves deciding which of these is the true ground phase. As shown in [Clou 98] μ is given by the distance along the line; this means that the nearer a coherence point is to Q, the higher is the corresponding ground-to-volume ratio μ. Remembering scattering physics, it is reasonable to expect that HV coherence
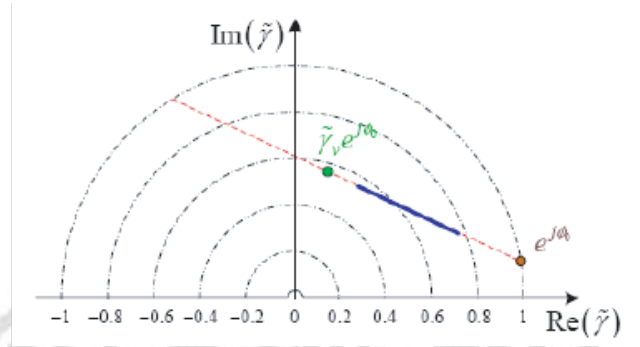
Figure 1.13: Coherence distribution.

channel will be ranked furthest away in distance from the ground phase point Q. To estimate the two remaining parameters, height and extinction, we use the estimation of ground phase ϕ and to find the intersection point between the coherence line and the curve corresponding to the height/extinction variations. By fixing the mean wave extinction σ at two different values and then varying the height, we obtain two different loci. Where the curve intersects the line, we have a candidate γ_v point. This becomes our estimation of the volume coherence $\hat{\gamma}_{est}$. From the baseline data we can estimate the vertical wave number k_z and then pre-calculate a look-up table (LUT) of γ_v as a function oh height h_v and wave extinction σ. By comparing $\hat{\gamma}_{est}e^{-j\phi}$ with the LUT, we can finally have an estimation of the height and extinction. We have to consider that this approach is based on a fitting algorithm of noisy data and it is possible that sometimes it gives non-physical solutions ([Clou 03], [Clou 98]). Moreover, in a real case, a volume scatterer such as a forest, does not show a so simple structure; usually there are more than one layer of certain ticknesses. Anyway, we have to notice that POLInSAR is able only to determine just the phase centre for each layer. Moreover, we are not sure that each layer as a polarimetric signature orthogonal with the other ones. The estimation process has problem of stability because is based on an estrapolation algorithm, therefore the problem should be ill-conditioned. In conclusion, polarimetric SAR interferomtery is able to estimate the height only of three different scattering process. However if a same scattering mechanism is distributed over different heights this tecnique fails because it is not able to split the received signal into different contributions.

1.4 SAR Tomography

Tomographic techniques are well known to have real three-dimensional imaging capabilities ([Reig 01]), in particular in medical applications (Computer Aided Tomography). In the case of SAR the tomographic acquisition process as well as the data processing are to be extended in a suitable way. It has been shown in Subsection 1.1.1, that for a fixed azimuth position x, the received SAR signal $s_r(t)$ under a given off-nadir angle θ is a convolution of the complex reflectivity $\rho(y, z)$ with the transmitted signal $s_t(t)$. Therefore, its spectrum can be expressed in terms of the FOURIER-transforms of the signal $\tilde{S}_r(w)$ and the reflectivity $\tilde{R}(k_y, k_z)$:

$$\tilde{S}_r(w) = \tilde{S}_t(w)\tilde{R}(k_y, k_z) \ , \quad with \ \ k_y = \frac{2w}{c}\sin(\theta), \ \ k_z = \frac{2w}{c}\cos(\theta) \ . \quad (1.47)$$

Spectra of images acquired from different positions (i.e. with different off-nadir angles θ) contain different slices of the spectrum of the reflectivity $\tilde{R}(k_y, k_z)$. By using a series of tracks, in this way a knoledge about a two dimensional area of the reflectivity function $\rho(y, z)$ can be reconstructed from this spectrum. This procedure corresponds to the formation of a second synthetic aperture in the normal direction, which is oriented perpendicular to the line-of-sight and azimuth direction (see Figure 1.14). It can also be interpreted as a multi-baseline interferometer with the number of tracks beign much greater than two. The multi-baseline imaging geometry is the technique adopted in the following. This imaging technique allows multiple
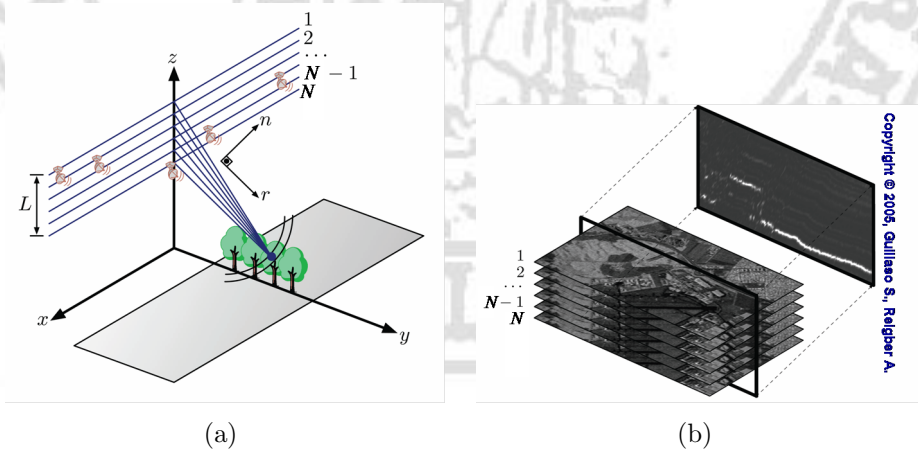

Figure 1.14: (a) Principle of multibaseline SAR tomography. (b) Extraction of 3D profile from N SAR images.

phase center separation in the vertical (height) direction, leading to a full

3-D reconstruction of the imaged scene. Retrieval of volume structure information (e.g. forestry classification) and the solution of the layover problem are two of the most promising applications.

1.5 SAR and Forestry applications

Forests are a dominant biome of the earth and have an important impact on its economic and environmental well-being. Moreover, they are also a major store of carbon, regulator of climate and water flow, habitat for wildlife, and reservoir of ecological and biological diversity ([Mette 02]). For the reasons
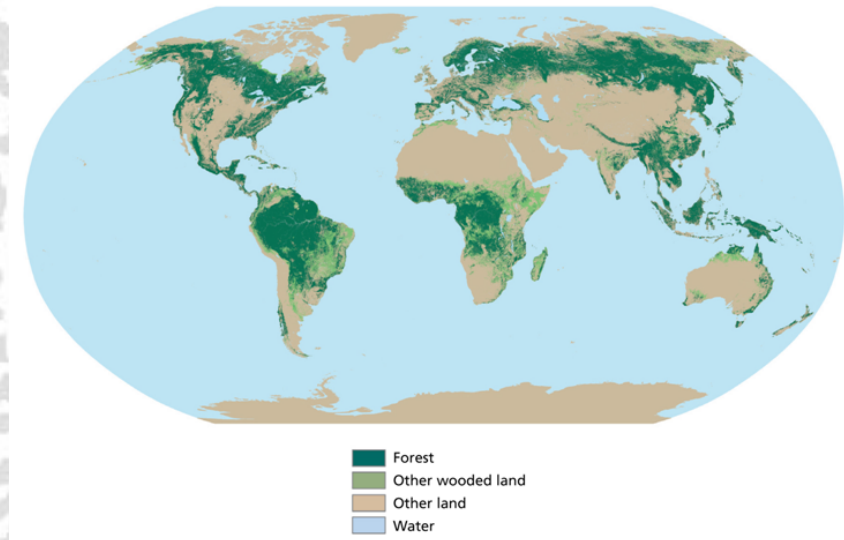
Figure 1.15: Global distribution of forests. Source: FAO 2006

explained above forest inventories are required to get informations about density, height, age and volume of them. The compilation of national forest inventories is very elaborate if we consider the large and often remote extension of forests. In this context, radar remote sensing can contribute to the monitoring of forests and to an understanding of ecosystem processes, providing information on some of the more important biophysical parameters. For example forest Biomass is a key parameter in understanding the carbon cycle and determining accurately global rates of carbon stocks (see figure 1.5). A methodology, based on forest height estimation from SAR data, was presented in [Mette 02]. Nowadays, global forest inventory and forest (above ground) biomass are critical topics in discussions about global climate change.

In particular forest biomass plays an important role in dynamic ecosystem change especially with respect to a reliable global Carbon-flux modelling. In the scenario of Kyoto protocol, this problem has not only an ecological dimension but also political ([Mette 02]). One promising approach to estimate
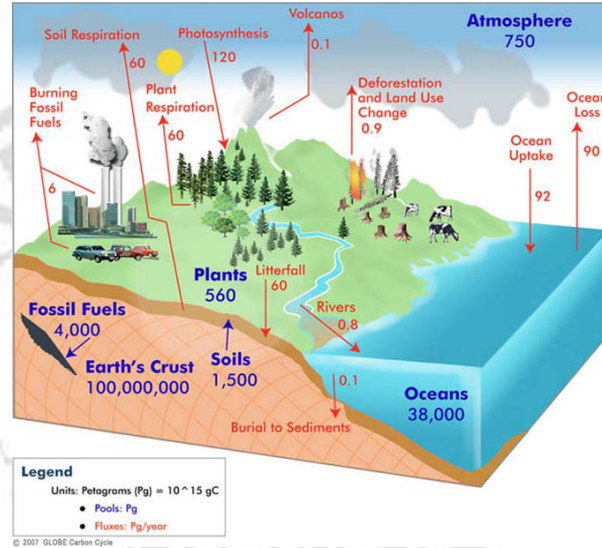

Figure 1.16: Global carbon cycle

forest biomass is via the *usable* stem volume (ger.: "Derbholz"-volume). The "Derbholz"-volume *Dh-vol* $[m^3/ha]$, is defined as the stem volume with more than 7 centimeters diameter and can be evaluated from

$$Dh - vol = basal\ area * average\ tree\ height * Fz_{DH} \qquad (1.48)$$

$$Dh - vol = forest\ height * Fz^* \qquad (1.49)$$

where *basal area* is the stem cross-section at $1.3m = breast height[m^3/ha]$, *average tree/forest height*$[m]$, Fz_{DH} the "Derbholz" form factor, a correlation factor, and Fz^* a modified form factor. Equation (1.48) is a forestry standard, while the second one is a modification that allows to relate "Derbholz"-volume to tree height directly without regarding basal area. Such equations are defined "allometric[5]" bacause they derive a certain size parameter from related parameters. The pysiological relevance of the allometric equation becomes evident, lies in the interpretation that any organ of the organism receives a part of the total growth energy that is proportional to the relative size. The standard forestry tables contain fixed ratios between basal area,

---

[5][gr.: *allos metros* - indirect measure. Allometry is the science concerned with the description of size relations in organisms.]

average tree height, Fz_{DH} and "Derbholz"-volume. The tables are organized in age classes and dinstiguish certain forest types. Fz_{DH} is therefore regarded as function of **age and forest type**. Since radar remote sensing systems measure height and not age, it makes sense to equation (1.49) and regard Fz^* as function of tree heights and forest type.The forestry tables describe forest types by 3 parameters:

1. **Stand conditions;**

2. **Forestry concept;**

3. **Species.**

An exact estimation of "Derbholz"-volume from tree heights is possible when these parameters are known. In a recent study, [Mette 02], it has been shown that when estimating "Derbholz"-volume from stand age, information about stand conditions is very important. On the other hand, when estimating "Derbholz"-volume from average tree height, the influence of stand conditions are negligible. This means that a specific height correlates with a specific biomass. This phenomenon is known as the extended law of Eichhorn ([Mette 02], [Mette 02]). A common allometric height biomass equation according to the rule of Eichhorn is:

$$B = 1.66 \cdot h_f^{1.58} \quad , \tag{1.50}$$

where B is the Biomass anh h_f is the forest height. It becomes evident we need to define "forest height". One promising parameter is the h_{100}, the average of the highest 100 trees per hectare. The reason is that it is probably close to the height that is extracted from a radar remote sensing system. This approach to estimate above ground biomass from forest heights has a first advantage to measure a significant higher biomass level. The second main advantage lies in the fact that instead of a direct relation of backscattered amplitude to biomass, important forest parameters as height, canopy density and underlying topography are directly estimated. These parameters are urgently required for a wide spectrum of forest applications apart from biomass estimation.

Chapter 2

SAR Tomography: state of the art

2.1 Formulation of the problem: parallel domains

To analyze the problem we consider a simple geometry where the observation domain and the investigation domain are parallel as we can see in figure 2.1. The locations of the tracks along the n direction is called *constellation*. L is the tomographic aperture, H is the maximum height of the volume, r_0 is the minimum range distance and d is the distance between two tracks, known also as the *baseline* ([Reig 00]). The information content of a SAR resolution cell is the projection of the 3-D scattering contributions into a 2-D plane. The lost dimension is related to the height of the scatterers that are occurring to form the radar echo that will be compressed into the resolution cell. Assuming that the scattering mechanism verifies the Born approximation[1], the received signal can be written as

$$s_r(\overline{n}) = \int_{-H/2}^{H/2} \rho(\overline{n}) e^{-j2\beta\sqrt{(\overline{n}-n)^2 + r_0^2}} d\overline{n} \qquad (2.1)$$

---

[1]The Born approximation represents the total scattered fields as the superposition of the scattered fields generated by the single scatterers, neglecting interactions between the scatterers themselves.
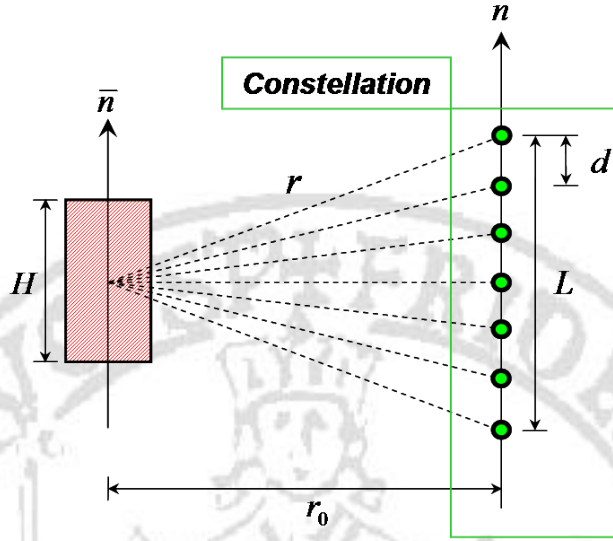
Figure 2.1: Tomographic constellation and geometry of the problem.

The phase term can be approximated

$$\sqrt{(\overline{n} - n)^2 + r_0^2}$$

$$\Updownarrow \tag{2.2}$$

$$r_0\sqrt{1 + \frac{(\overline{n}-n)^2}{r_0^2}} \approx r_0 \left[1 + \frac{(\overline{n} - n)^2}{2r_0^2} \right] = r_0 + \frac{(\overline{n} - n)^2}{2r_0}$$

Neglecting the quadratic phase terms the expression of the received signal is

$$s_r(\overline{n}) = \int_{H/2}^{-H/2} \rho(\overline{n})e^{-j2\beta\frac{\overline{n}n}{r_0}}\,d\overline{n} = \int_{H/2}^{-H/2} \rho(\overline{n})e^{-j2\frac{2\pi}{\lambda}\frac{\overline{n}n}{r_0}}\,d\overline{n} \tag{2.3}$$

We notice that there is a Fourier transform relation between the received signal and the reflectvity $\rho(\overline{n})$. Different approaches can be used to extrapolate from this relation the unknown reflectivity.

2.2 Spectral Analysis

The basic principle of tomographic SAR focusing is to perform an aperture synthesis in the n-direction by aid of the different flight tracks. It will be shown that for reasonable resolutions in height the distances between the

furthermost tracks can stay relatively small. In order to distinguish clearly between sensor and target coordinates, the latter are marked in the following by an overbar. Additionally, a simplified geometry, as shown in Fig. 1.14, will be used. It assumes equally spaced baselines and it neglects all projections related to the off-nadir angle θ, i.e. $\vec{n}$ is considered to have the same direction as $\vec{z}\,(\theta = 90°)$. In the real side-looking case, d would correspond to the baseline perpendicular to the **line-of-sight** (LOS) and $\vec{n}$ to a scatterer height of $\bar{h} = \bar{n}\sin(\theta)$. The two-way pathlength between the sensor at position n and a scattering element at height $\bar{n}_0$, with minimum range distance r_0, can be espressed as:

$$r(n, \bar{n}_0) = 2\sqrt{(r_0^2 + (n - \bar{n}_0)^2)} \simeq 2r_0 + \frac{(n - \bar{n}_0)^2}{r_0} \quad, \tag{2.4}$$

and the received signal s_r can be modelled as

$$s_r(n, \bar{n}_0) = \rho(\bar{x}_0, \bar{n}_0, \bar{r}_0)e^{-\frac{jk}{r_0}(n - \bar{n}_0)^2} \quad, \tag{2.5}$$

where $\rho(\bar{x}_0, \bar{n}_0, \bar{r}_0)$ denotes the complex reflectivity at the scene coordinate $(\bar{x}_0, \bar{n}_0, \bar{r}_0)$, and k the wavenumber $2\pi/\lambda$. The received signal consists of the complex reflectivity convolved with a quadratic phase function. This chirp signal is a function of the n-direction and has a zero frequency offset if $\bar{n}_0 = 0$. It shows a positive frequency offset if the height of the target is positive, and a negative offset if the height of the target is negative. The algorithm to process the tomographic signal is called 'SPECAN' and is based on the assumptions that the range migration is very small and the received signal has a quadratic phase modulation independent from its position in the scene. The first step in the SPECAN is to compensate the quadratic phase variation by multiplying the received signal s_r by a complex conjugate quadratic phase function. This operation is denoted as 'deramping ' (see Fig. 2.2). By multiplying the received signal with a deramping function

$$u(n) = e^{\frac{jk}{r_0}n^2} \tag{2.6}$$

a demodulated signal s_d can be obtained:

$$s_d(n, \bar{n}_0) = \rho(\bar{x}_0, \bar{n}_0, \bar{r}_0) * e^{-\frac{jk}{r_0}(\bar{n}_0^2 - 2n\bar{n}_0)} \quad. \tag{2.7}$$

The spatial frequency k_n of the deramped signal s_d is no longer dependent on the n-position; it depends only on the height $\bar{n}_0$ of the occurring scattering processes

$$k_n(\bar{n}_0) = \frac{\partial arg(s_d)}{\partial n} = \frac{2k\bar{n}_0}{r_0} \tag{2.8}$$
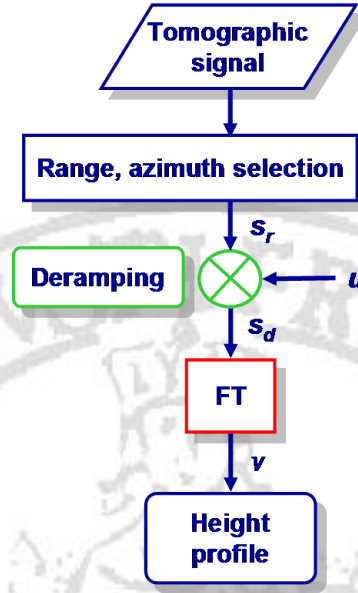
Figure 2.2: Block diagram of SPECAN algorithm.

The final step in the SPECAN algorithm is to perform a spectral analysis by means of a Fast Fourier Transform (FFT). According to equation (2.8) the k_n-domain (height frequency domain) is directly related to the spatial $\bar{n}$-domain in the object space. The desired image result $v(\bar{n}, \bar{n}_0)$ is, therefore, equal to the FOURIER-transforms of the deramped signal in the n-direction $S_d(k_n, \bar{n}_0)$

$$v(\bar{n}, \bar{n}_0) = S_d(k_n, \bar{n}_0) = \rho(\bar{x}_0, \bar{n}_0, \bar{r}_0) e^{-\frac{jk}{r_0}\bar{n}_0^2} \int_{-L/2}^{+L/2} e^{\frac{2jk}{r_0}(\bar{n}-\bar{n}_0)n} \, dn \qquad (2.9)$$

and resolving the integral we obtain

$$v(\bar{n}, \bar{n}_0) = \rho(\bar{x}_0, \bar{n}_0, \bar{r}_0) \, L \, e^{-\frac{jk}{r_0}\bar{n}_0^2} \, sinc\left(\frac{kL}{r_0}(\bar{n}_0 - \bar{n})\right) \quad . \qquad (2.10)$$

From the width of the sinc-function, the geometric resolution in the n-direction results as

$$\delta_{\bar{n}} = \frac{\lambda r_0}{2L} \quad . \qquad (2.11)$$

The bigger is the tomographic aperture the better is the resolution. We have assumed until now that the signal is continously measured at all positions in the receiving plane. In the real case, for the feasibility condition, only a certain number of tracks can be flown.
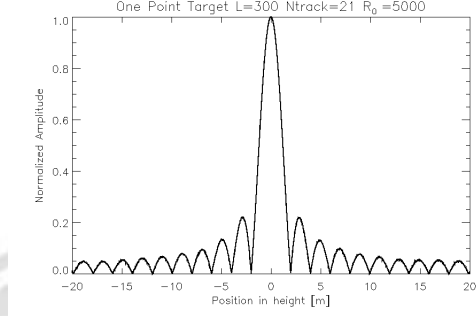
Figure 2.3: Reconstruction of one point target with a constellation of 21 tracks, a tomographic aperture of 400m and the minimum range distance of 5000m.

For this reason, we have to take care that the illumination path is properly sampled in order to avoid height ambiguities. Conseguence of this is that the sampling distance d must be sufficiently small to fulfil the NYQUIST-criterion for the spatial bandwidth of s_d. If this can not be fulfilled, high sidelobes and ambigiuties will occur in the image. The sampling distance d, which is necessary for unambiguous imaging, depends on the total height H of the examined volume:

$$d \leq 1/B_{s_d} = \left| -2\pi \left(\frac{\partial arg(s_d)}{\partial n} \right)^{-1} \right| = \frac{\lambda r_0}{2H} \quad . \tag{2.12}$$

In Fig. 2.4(a) the two sincs are distinguished but the resolution is limited, and the sinc functions are not thin.

(a)   (b)
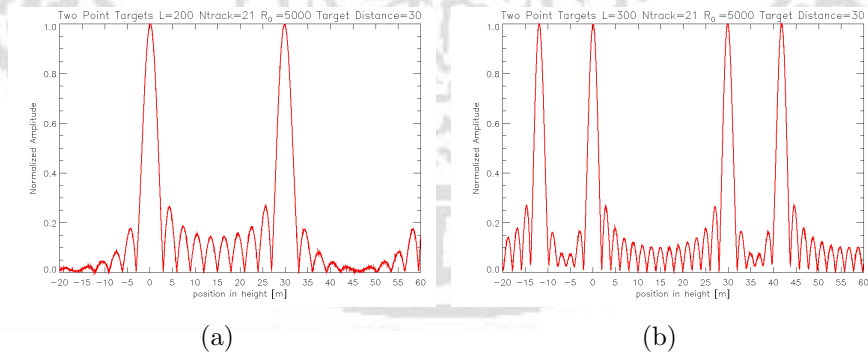
Figure 2.4: Reconstructions with 2 points target at distance of 30m, with (a) the full system of 21 tracks and a baseline of 10m (b) the full system of 21 tracks and a baseline of 15m.

The drawback of SARTom is that to obtain a good resolution and avoid

ambiguities a large number of tracks is needed implying a big cost for the system. For this reason it becomes critical to find new approach for the reduction of the constellation.

2.3 Alternative approaches for SARTom

Many different approaches have been recently investigated to overcome the drawbacks of Fourier analysis ([Nann 08], [Nann 09]). In this work we present due approaches relating to different categories. The first one is a non parametric method, called CAPON and the second one is a parametric approach known as MUSIC. In general, all high resolution methods are based on a covariance matrix formulation defined as

$$\underline{\underline{R}} = \langle s_r s_r^\dagger \rangle \text{ which is estimated by } \hat{\underline{\underline{R}}} = \sum_{i=1}^{N_S} s_r s_r^\dagger \ , \tag{2.13}$$

where $N_S I$ represents the number of samples used to generate the covariance matrix $\hat{\underline{\underline{R}}}$. The condition $N > I$ is necessary in order to avoi a singular matrix $\hat{\underline{\underline{R}}}$. CAPON method is a classical approach based on beamforming/spectral estimation method. The main idea is to focus the system on a certain height, corresponding to the height of a scatterer. To do that, the range of valid heights is scanned in order to find the maximum of power. The estimate power given by CAPON, $\hat{P}_C(\overline{n})$, is function of the height $\overline{n}$:

$$\hat{P}_C(\overline{n}) = \frac{1}{\underline{a}(\overline{n})^\dagger \hat{\underline{\underline{R}}}^{-1} \underline{a}(\overline{n})} \ , \tag{2.14}$$

where $\underline{a}(\overline{n})$ is the steering vector. It must be mentioned that the CAPON estimator corresponds to a minimisation of the received power in all direction except those of the observed scatterer. When we use CAPON no estimation of the number of dominant scatterers is needed. The second category is based on the principle of subspace estimation. The most known subspace method is MUSIC. The idea is to identify two different subspaces: *signal* and *noise* subspace. Then using an eigendecomposition, the observed covariance matrix is decomposed, $\hat{\underline{\underline{R}}} = \hat{\underline{\underline{E}}} \, \hat{\underline{\underline{\Gamma}}} \, \hat{\underline{\underline{E}}}^\dagger$, where $\hat{\underline{\underline{E}}}$ represents the matrix of eigenvectors of $\hat{\underline{\underline{R}}}$, and $\hat{\underline{\underline{\Gamma}}}$ is a diagonal matrix formed with the eigenvalues of $\hat{\underline{\underline{R}}}$. After that the eigenvector space is decomposed into the two subspaces, the *signal* subspace $\hat{\underline{\underline{E_S}}}$, and the *noise* subspace $\hat{\underline{\underline{E_N}}}$, with $\hat{\underline{\underline{E}}} = \hat{\underline{\underline{E_S}}} \, \hat{\underline{\underline{E_N}}}$. It is possible then to scan a functional that represents the projection of the steeering vectors themselves

into the noise subspace. If the steering vector is matching a direction where a scatterer is located, then its projection into the noise subspace will be zero. The functional of the MUSIC $\hat{P}_M(\overline{n})$, is given by:

$$\hat{P}_M(\overline{n}) = \frac{1}{\underline{a}^\dagger(\overline{n}) \left(\underline{\hat{E}_N} \, \underline{\hat{E}_N}^\dagger \right) \underline{a}(\overline{n})} \tag{2.15}$$

Using MUSIC we need an estimation of the number of dominant scatterers. The MUSIC algorithm has been used for SAR Tomography to estimate the mean phase center of the volumetric target and its width. This algorithm is often defined as pseudobeamforming technique because it gives information about the position of the phase centers of scatterers, rather than the measure of their backscattered power. In particular, in [Nann 08] it has been proposed a new method to reduce the number of tracks with an equivalent resolution of 3m.

Figure 2.5: Full polarimetric SAR image with R(HH)-G(VV)-B(HV) color coding. The forested area is analyzed along the cut represented by the straight line.

The data has been acquired with E-SAR, in L-band during one day in September 2006 over Dornstetten (Germany). The acquisition geometry is nominally regular horizontal grid of 21 tracks with an average baseline of 20m. In Fig. 2.3 we can see a SAR polarimetric image of the forest in Dornstetten. In Fig. 2.6(a) we can see the reconstruction obtained with CAPON method using a constellation of 21 tracks. In Fig. 2.6(b) we can see the
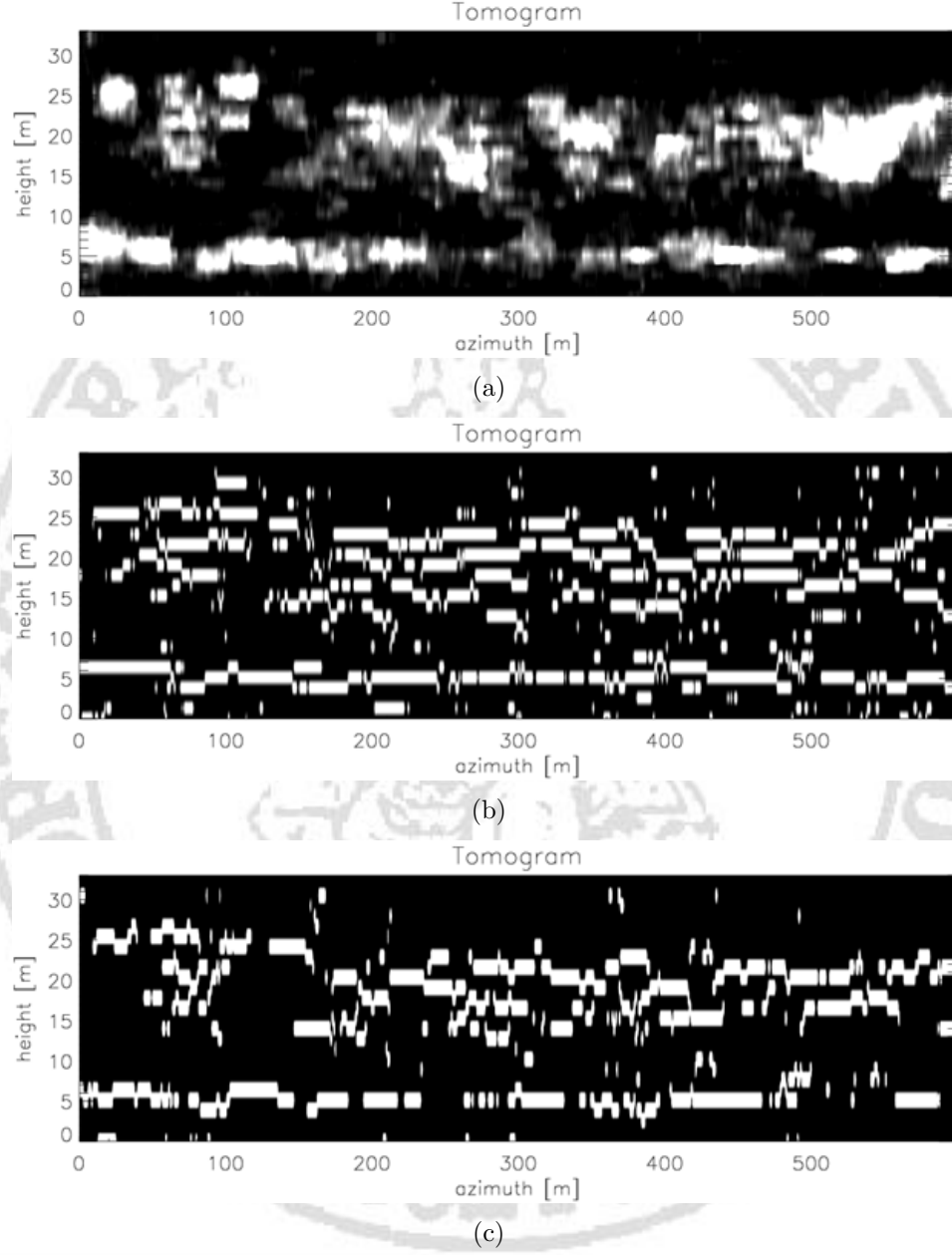
Figure 2.6: Tomograms of a forested area obtained using the full tomographic aperture and N = 21 tracks with (a) CAPON beamforming and (b) MUSIC algorithm. (c) Tomogram obtained using the reduced aperture and N = 8 tracks by means of the MUSIC algorithm.

reconstruction obtained with the full constellation using MUSIC. They end up with a constellation with 8 tracks as we can notice in the Fig. 2.6(c). Finally, they have done an average along the azimuth as we can see in Fig. 2.3. The two distributed components related with ground and canopy have
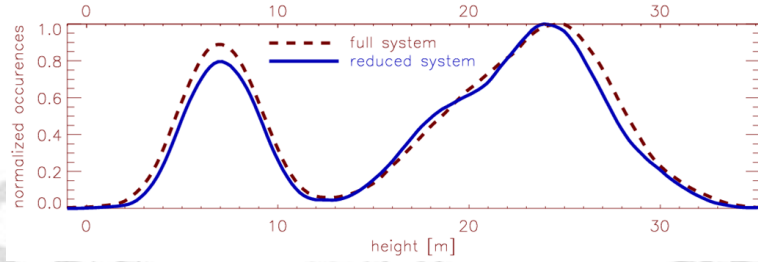
Figure 2.7: Normalized average of the profiles along azimuth of (dashed line) Fig. 2.6(b) and (solid line) Fig. 2.6(c).

a Gaussian shape. This result is consistent with the assumed forest model and the estimated averaged tree height. Therefore for the following analysis we will assume Gaussian shapes for the ground and canopy responses and we will use a reduce system with 8 tracks.

Chapter 3

SVD optimisation and parametric inversion

3.1 SVD inversion

In this section we propose a different approach for SAR tomography, by formulating the problem in a linear inverse problem framework [Bert 98]. Equation (2.3) shows the relation between the unknown $\rho(\overline{n})$ and the data $s_r(\overline{n})$; the data is not continous but is discrete because it is acquired building a constellation of N tracks. This means that for each general track k the equation (2.3) becomes:

$$s_r(\overline{n})_k = \int_{-H/2}^{H/2} \rho(\overline{n}) e^{-j\frac{4\pi}{\lambda}\frac{\overline{n}n_k}{r_0}} \, d\overline{n} \qquad (3.1)$$
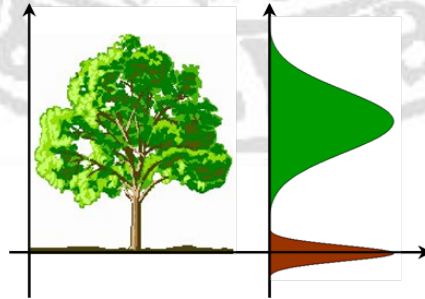
Figure 3.1: Ground and canopy responses

This means that the reconstruction is obtained by solving a semidiscrete linear inverse problem. Starting from measured discrete data we solve the problem finding the 3-D density function. To solve a linear inverse problem we have to discretize the operator. This operation involves two step. A first step is the discretization of the unknown; this step implies the choice of basis functions to represent the unknown and is very crucial. In a recent work [Nann 08] it has been shown how ground and canopy appear as two Gaussians contributions. This allows us to use Gaussians to make a Gaussians expansion to represent the unknown. This choice permits us to modulate the resolution
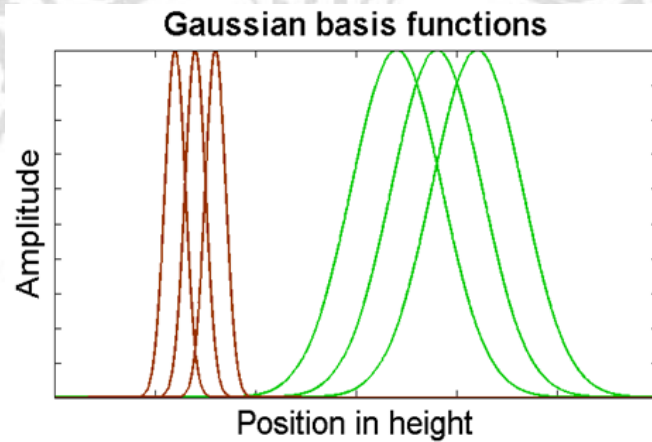
Figure 3.2: Examples of six basis Gaussians functions

varying our basis functions and to add a-priori information into the model. If we define the number of basis functions, N_b we can write the density as

$$\rho(\overline{n}) = \sum_{i\,=\,1}^{N_b} c_i\, b_i(\overline{n})\,, \ \ where \ \ \underline{b}(\overline{n}) = [b_1(\overline{n}), b_2(\overline{n}), ..., b_{N_b}(\overline{n})] \ . \qquad (3.2)$$

The second step regards the sampling of the data. This operation consists at finding a constellation with a limited number of tracks. The use of a reduced number of tracks in combination with the use of Gaussians function to represent the unknown leads to an irregular constellation. Moreover the geometry in the real case is a bit different from the case of parallel domains (see Figure 3.3). In this case we have not got two parallel domains but we can reconduct to the case of parallel domains adding a right phase to the reconstruction.
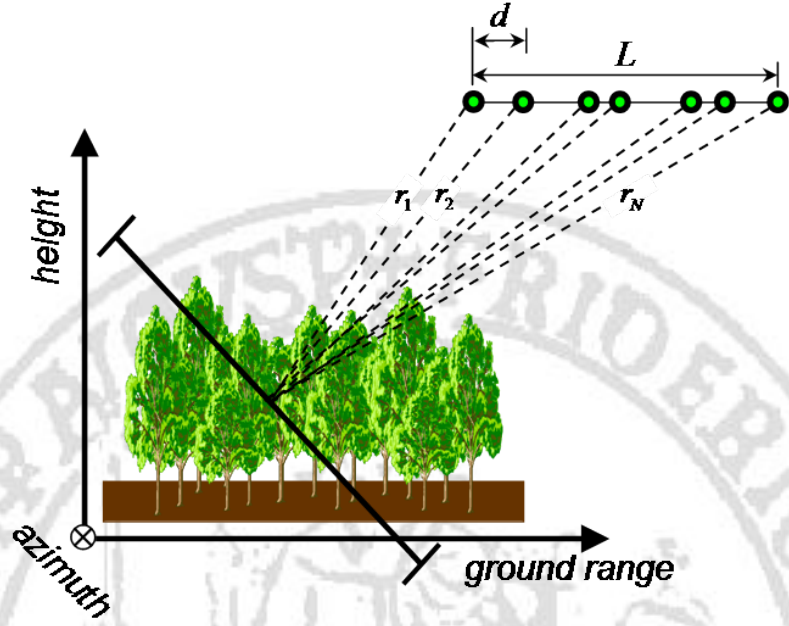
Figure 3.3: Geometry of SAR tomography in the real case

Collecting all the measured data from an certain constellation of N tracks, the mathematical expression of tha data is

$$\underline{s}_r = [s_{r_1}, s_{r_2}, ..., s_{r_N}], \ \Rightarrow \ \underline{s}_r \in \mathbb{C}^N \ . \tag{3.3}$$

The measured data is a complex vector of N elements. If we want to obtain the vector of weight coefficients for the basis functions to represent the unknown, the problem consists of the following inverse problem:

$$\underline{s}_r = \underline{\underline{B}}\,\underline{c}, \ \ \underline{c} = [c_1, c_2, \dots, c_{N_b}] \ , \tag{3.4}$$

where $\underline{c}$ is the vector containing the weight coefficients. $\underline{\underline{B}}$ is a matrix $N_b x N$ and the generic element of the matrix is:

$$B_{ij} = \int_{-H/2}^{H/2} b_j(\overline{n}) e^{-j2\beta \frac{n\overline{n}_i}{r_0}} \, dn \tag{3.5}$$

Thanks to the **S**ingular **V**alue **D**ecomposition (SVD), it is possible to decompose the matrix $\underline{\underline{B}}$ as the product of three matrices

$$\underline{\underline{B}} = \underline{\underline{U}}\,\underline{\underline{S}}\,\underline{\underline{V}}^\dagger \ , \tag{3.6}$$

36

where the superscript † stands for the transpose conjugate of a matrix. $\underline{\underline{S}}$ is called singular matrix and is a diagonal matrix

$$\underline{\underline{S}} = \begin{bmatrix} \sigma_1 & 0 & \cdots & \cdots & 0 \\ 0 & \sigma_2 & 0 & \cdots & \vdots \\ \vdots & 0 & \ddots & 0 & \vdots \\ \vdots & \cdots & \cdots & \ddots & 0 \\ \vdots & \cdots & \cdots & \cdots & \sigma_{N_b} \\ \vdots & \cdots & \cdots & \cdots & 0 \\ \vdots & \cdots & \cdots & \cdots & \vdots \\ 0 & \cdots & \cdots & \cdots & 0 \end{bmatrix} \tag{3.7}$$

and the vector $\underline{\Lambda} = [\sigma_1, \sigma_2, ..., \sigma_{N_b}]$ is the vector containing the singular values. The operator $\underline{\underline{B}}$ admits a singular system defined by the following problems:

$$\begin{cases} \underline{\underline{B}} \, \underline{v}_i & = & \sigma_i \, \underline{u}_i \\ \underline{\underline{B}}^\dagger \, \underline{u}_i & = & \sigma_i \, \underline{v}_i \end{cases} \tag{3.8}$$

where $\underline{v}_i$ is the i-th element of the set of singular functions and $\underline{u}_i$ is the i-th element of the set of singular vectors. Using the following expressions

$$\underline{c} = \sum_{i=1}^{N_b} c_i \underline{v}_i$$

$$\Downarrow$$

$$\underline{s}_r = \underline{\underline{B}} \, \underline{c} = \sum_{i=1}^{N_b} c_i \underline{\underline{B}} \, \underline{v}_i = \sum_{i=1}^{N_b} c_i \sigma_i \underline{u}_i \tag{3.9}$$

$$\Downarrow$$

$$s_{r_i} = \sigma_i c_i \quad \Rightarrow \quad c_i = \frac{s_{r_i}}{\sigma_i}$$

and the relation $b_i = \left(\underline{\underline{U}}^\dagger s_r \right)_i$ we obtain:

$$\underline{c} = \sum_{i=1}^{N_b} \frac{1}{\sigma_i} \left(\underline{\underline{U}}^\dagger \underline{s}_r \right)_i \underline{v}_i \tag{3.10}$$

When we use SVD to reconstruct the object function γ we should take care when low singular values are present, since they could amplify the noise component in the inversion process and introduce instability. For example, denoting with $\delta\beta_i$ an error on the data we have:

$$\underline{c} = \sum_{i=1}^{N_b} \alpha_i \, \underline{u}_i \quad \underline{s}_r = \sum_{i=1}^{N_b} \beta_i \, \underline{v}_i$$

$$\underline{\underline{B}} \left(\sum_{i=1}^{N_b} \alpha_i \, \underline{u}_i \right) = \sum_{i=1}^{N_b} \alpha_i \underline{\underline{B}} \, \underline{u}_i = \sum_{i=1}^{N_b} \alpha_i \sigma_i \, \underline{v}_i = \underline{s}_r = \sum_{i=1}^{N_b} \beta_i \underline{v}_i \qquad (3.11)$$

$$\beta_i = \alpha_i \sigma_i \;\Rightarrow\; \alpha_i = \frac{\beta_i}{\sigma_i}$$

The error on the data and on the unknown will be

$$\overline{\beta}_i = \beta_i + \delta\beta_i$$

$$\overline{\alpha}_i = \frac{\beta_i}{\sigma_i} + \frac{\delta\beta_i}{\sigma_i} \qquad (3.12)$$

From equation (3.12) the error $\delta\beta_i$ could be amplified if σ_i is a low singular value leading to a large error on $\overline{\alpha}_i$. This effect is referred to as noise propagation; due to it we prefer to look for a reliable solution restricting the solution space to a subspace spanned only by singular functions corresponding to the singular values that are over a threshold representing the noise level. This scheme is called **t**runcated **SVD** (**TSVD**) [Bert 98]. If we denote with $\overline{N}_b$ the number of singular values above the threshold equation (3.10) becomes:

$$\underline{c} = \sum_{i=1}^{\overline{N}_b} \frac{1}{\sigma_i} \left(\underline{\underline{U}}^\dagger \underline{s}_r \right)_i \underline{v}_i \qquad (3.13)$$
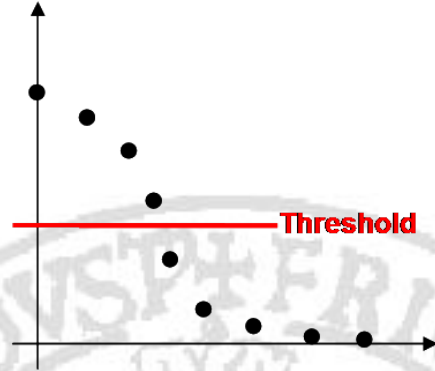
Figure 3.4: Truncated singular values

An example is now proposed to show the potentiality of TSVD. Let us consider an actual distribution of two gaussians and choose a constellation with two tracks and a baseline of 20m.

(a) Gaussian basis functions
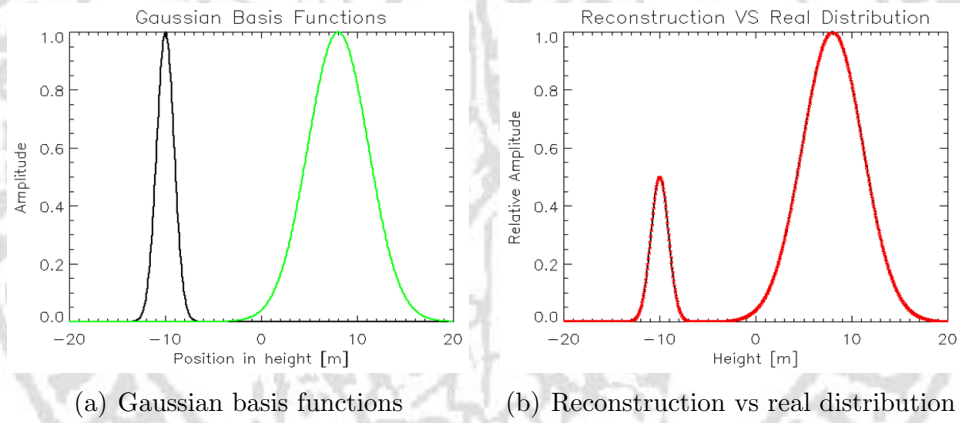

(b) Reconstruction vs real distribution

Figure 3.5: Example of TSVD with 2 tracks

The basis functions will be two Gaussians with the same positions and variance of the actual distribution but the amplitudes don't match. Adding noise with an SNR equal to 15dB we invert the problem with TSVD obtaining a reconstruction (red line) that completely matches the actual distribution (black line). This means if I want to evaluate two unknowns - in our case the amplitudes of the Gaussians of the real distribution - we need only two tracks.

3.2 SVD for constellation optimisation

When we use a low number of samples for the data, the problem becomes ill-conditioned. Because we are not obliged to use a uniformly spaced passes, the main idea of this work was to implement an algorithm to find the "best" constellation i.e., a constellation providing the "best" conditioning of the matrix to be inverted. This is equivalent to searching for the constellation with the highest trend of the singular values. In combination with the Truncated
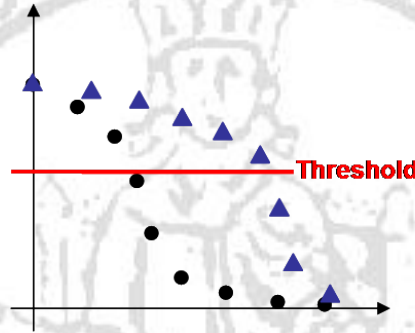
Figure 3.6: Singular values optimisation

SVD and a reduced number of tracks, choosing the optimum constellation allow us to include a bigger number of singular values to invert the problem. In this way we get more information to retrieve the height profile, as we can see also in the Figure 3.6. We choose a certain set of Gaussian functions (in our case is equal to six). For each constellation we obtain a linear problem

$$\underline{s}_r = \underline{\underline{B}}\,\underline{c} \quad . \tag{3.14}$$

Using SVD we decompose the matrix $\underline{\underline{B}}$, obtaining the vector with the singular values $\underline{\Lambda} = [\sigma_1, \sigma_2, \ldots, \sigma_{N_b}]$. The aim of the algorthm is to find the constellation with the highest seguence of σ_i. In the following picture we present the block diagram of the algorithm implemented in IDL:

We can notice that the algorithm minimizes a functional related to the inverse of the sum of the normalized singular values:

$$constellation : F = \min F \,, \quad F = \frac{1}{\displaystyle\sum_{i=1}^{N_b} (\sigma_i/\sigma_1)} \quad , \tag{3.15}$$

where N_b is the number of basis functions. Starting from a guess constellation the algorithm gives us the numerical solution of the functional to minimize.
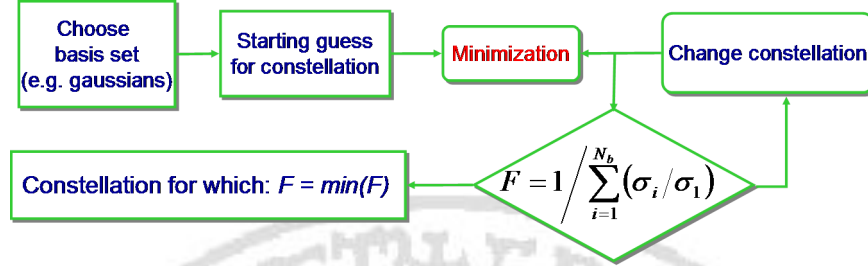
Figure 3.7: Block diagram of singular values optimisation

We have started from a uniform 8 tracks constellation and the solution are 8 nonuniformly spaced passes. To verify the robustness of the method we have also started from a non regular 8 tracks constellation with the same total aperture of 140m. In both case the final optimised constellation is the same. This algorithm has been implemented for simulations. In the case of real data we have already a data set. We have flown with a 21 regular constellation. The constellation of 21 tracks has an aperture of 400m and a baseline of 20m. It is the same constellation acquired in the forest of Dornstetten in September 2006, used by Nannini in his work ([Nann 08]). In this case we are not able to find the constellation of 8 tracks with any grade of freedom. We are limited to choose the position from the 21 already flown. For this reason we have done an optimisation choosing the "best" 8 passes over the 21 already flown. As we have done in the case of simulated data we have choosen a set of basis function and the algorithm gives us the constellation that implies the optimum conditioning of our inverse problem. Fixed the constellation, the choice of a certain set of basis functions allow us to overcome the problem of inversion adding a-priori information into the model. Because the scene may vary (for example the height of forest could change), we need to find a constellation that is the "best" possible in average. If we decide to flight over certain passes based on the choice of Gaussian functions as basis functions, we could be in a situation where the a-priori information inserted into the model are too strong. To free ourselves from the a-priori information added to the model, we have decided to use several sets of basis functions. All sets are constituted of Gaussian functions with different position and variance. The optimisation algorithm now must minimized a functional that is the mean of all the 20 functionals related to each set of basis function

$$F = \frac{1}{20} \sum_{k=1}^{20} F_k \quad , where \ F_k = \sum_{i=1}^{\overline{N_b}} (\sigma_i/\sigma_1) \ . \qquad (3.16)$$
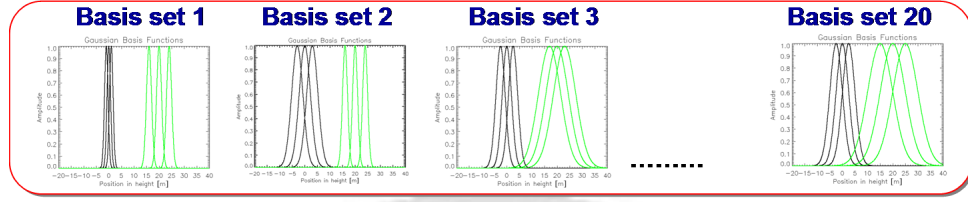
41

Figure 3.8: Representation of several sets of Gaussian basis functions

In this way we obtain a constellation that is the "best" in average. In the following figure we can see a simple block diagram of the constellation optimisation with 20 sets of basis functions. Summarising, we can say that
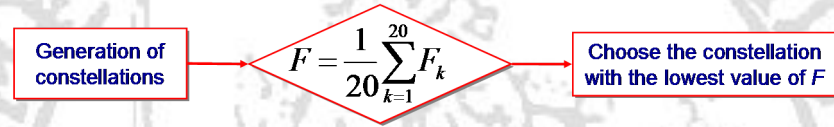

Figure 3.9: Block diagram of optimisation with 20 sets of Gaussian basis functions

the SVD inversion does not give a reconstruction that is totally independent from the a-priori information, but the SVD tool to optimize the constellation is a good candidate for a strategy to design a constellation for a campaign. In this scenario our idea is to use SVD to design the constellation and to use a more stable and precise approach for the inversion.

3.3 Parametric inversion

An alternative method proposed in this work to retrieve the height profile is based on a parametric inversion. Referring to the configuration with N parallel tracks, presented in the previous chapter, If we define six parameters related to the ground and canopy, for each sestuple we obtain a measured density:

$$X = (x_1, x_2, x_3, x_4, x_5, x_6) \quad X \in \Re^6$$

$$\underline{\gamma}_{meas} = \overline{x}_1 e^{-\overline{x}_5(x_3 - \overline{x}_3)^2} + \overline{x}_2 e^{-\overline{x}_6(x_4 - \overline{x}_4)^2} \quad , \tag{3.17}$$

where $\overline{x}_1, \overline{x}_2$ denote the amplitudes of ground and canopy respectively, $\overline{x}_3, \overline{x}_4$ the position of the gaussians related to ground and canopy and $\overline{x}_5, \overline{x}_6$ their

variances. For the generic track k, the measured backscattered signal will be:

$$s_{meas_k} = \int_{-H/2}^{H/2} \left(\overline{x}_1\, e^{-\overline{x}_5(n-\overline{x}_3)^2} + \overline{x}_2\, e^{-\overline{x}_6(n-\overline{x}_4)^2} \right) e^{-j2\beta\frac{n\overline{n}_k}{r_0}}\, dn \quad . \qquad (3.18)$$

This kind of model-based inversion relies on an optimisation procedure in which the density in the height direction is reconstructed by optimising the following **objective function**:

$$F(x_1, x_2, x_3, x_4, x_5, x_6) = ||\underline{s}_{meas} - \underline{s}_r||^2 \qquad . \qquad (3.19)$$

The value of this function indicates the closeness between the measured data and the backscattered signal as predicted following an estimate of the unknown parameters $x_1, x_2, ..., x_6$. In general, because the forward model is nonlinear, the resulting objective function may have several optima.

This kind of inversion methods yield the correct results if they converge to the global optimum of the objective function. A first step to ensure the convergency to the global minimum, is to incorporate *a priori* information in the definition of the objective function. Defining the minimum and maximum values for all the six parameters we can define a subspace Ω of $\Re^6$ where to search for the global minimum. The problem now is to find the sestuple:

$$(x_1^*, x_2^*, x_3^*, x_4^*, x_5^*, x_6^*) : F(x_1^*, x_2^*, x_3^*, x_4^*, x_5^*, x_6^*) = \min_{\Omega \subseteq \Re^6} ||\underline{s}_{meas} - \underline{s}_r||^2 \quad . \quad (3.20)$$

However, local optimisation methods such as conjugate gradient method don't ensure the convergence to the true solution, which corresponds to the global optimum. One way to overcome this problem is to apply global optimisation methods, such as **s**imulating **a**nnealing (**SA**), and **g**enetic **a**lgorithms (**GA**). The main drawbacks of these approaches regard their low efficiency in terms of computation time and are low accuracy in locating the exact solution [Nakh 99]. Therefore in this work we use a **m**ulti**l**evel **s**ingle-**l**inkage method (**MLSL**), which incorporates a local optimisation method into the global search.

3.3.1 Global Optimisation of objective function

Multi-level single linkage method is a stochastic iterative method based upon some kind of random sampling in the feasible domain Ω. To avoid repetition of local searches, occurring in the case of a simple Random Search method, MLSL include an adaptive search strategy, sample clustering, and a statistical stopping rule as enhancements to the basic scheme of pure random sampling. The procedure of MLSL for the k-th iteration is the following:

1. Generate P sample points drawn from a uniform distribution over Ω, and calculate the corresponding functional values at these points. Add P points to the (initially empty) set of sample points;

2. Sort the whole sample of Pk points in order od decreasing function value, and select the ξPk points with the smallest function values, where ξ is any fixed number in $(0, 1]$; the resulting sample is called **reduced sample**;

3. Select start points from the reduced sample points for local searches. The selection will be discussed later;

4. Perform local minimizations from the selected starting points;

5. If the stopping rule is satisfied, the lowest local minimum is taken as the global minimum, otherwise go to Step 1.

In Step 3. at the k-th iteration each reduced sample point $\overline{X}$ is selected as a starting point for a local minimization provided that the starting point has not been used at a previous iteration and that there is no sample point $\overline{Y}$ within the critical distance $d(k)$ of $\overline{X}$ with $F(\overline{Y}) < F(\overline{X})$. The critical distance is given by

$$d(k) = \pi^{-1/2} \left[\Gamma \left(1 + \frac{M}{2} \right) \Psi(\Omega)\, \tau\, \frac{\log kP}{kP} \right]^{1/M} , \qquad (3.21)$$

where Γ stands for the gamma function, $\Psi(\Omega)$ denotes the Lesbegue measure of Ω and τ is a positive constant. $M = dim(X) = 6$ is the dimension of the space of objective function.

In [Rinnoo 87] the following theoretical properties have been proven:

- When $\tau > 0$, all local minima of $F(\overline{X})$ will be found within a finite number of iterations with probability one;

- When $\tau > 4$, the total number of local searches started by the MLSL method will be finite with probability one even if the sampling continues forever. In our reconstructions, τ is set to six.

From a computational point of view varius authors confirm the numerical feasibility of this approach even if they point out some weaknesses such as the necessity of storing the whole sample and the decision about local searches. In fact, as the threshold $d(k)$ is decreasing with k, the decision of not starting a local search from a point might be revised in a subsequent iteration. For this reason, the choice of P, the sample size of each cycle, is quite critical as too small value would imply too many revisions of previous decisions, while a choice of a big sample size might produce a waste computational effort due to the high number of function evaluations required. Anyway, this algorithm is amenable to be parallelized to reduce the computational effort and show much more flexibility as compared to the SVD inversion. Moreover, while the convergence of GA and its variants to the global minimum is guaranteed in a weak probabilistic sense, in the case of MLSL there exists a probabilistic guarantee to find the global minimum of a function within a finite number of local searches [Rinnoo 87]. Finally, the method presented is based on the assumption that the function and its gradient are continous.
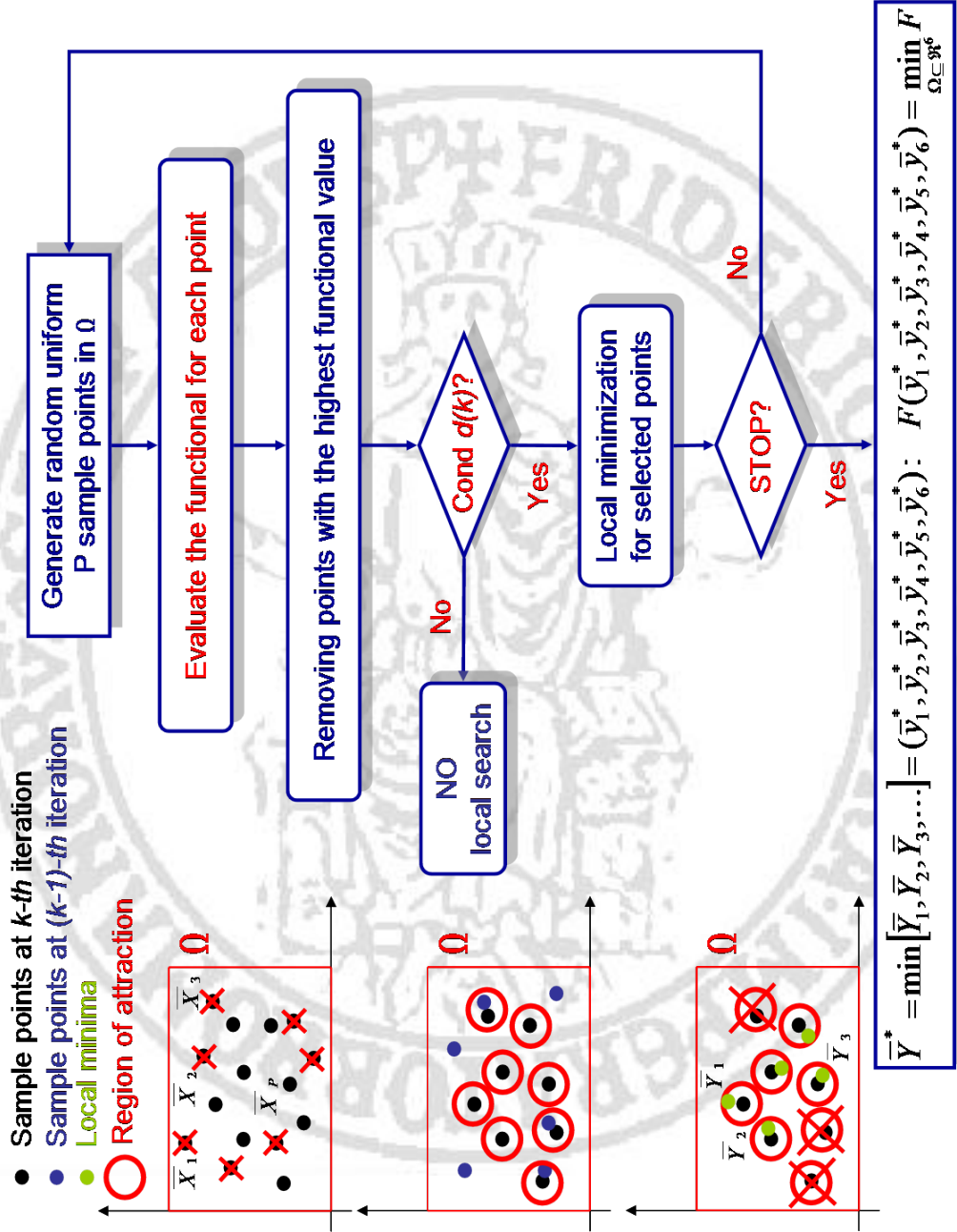
Figure 3.10: Block diagram of MLSL algorithm

Chapter 4

3D Reconstruction: numerical and experimental results

4.1 Simulated data analysis

In this section we present results of simulations performed using SVD inversion and parametric inversion. In both cases simulations has been done firstly with the full constellation (21 tracks) and later with the reduced system (8 tracks).

4.1.1 SVD inversion: simulated results
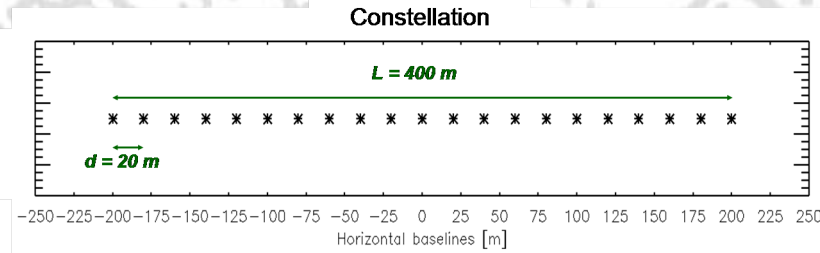
Figure 4.1: 21 tracks constellation

The first simulation arranged with SVD inversion has used 21 tracks represented in the figure 4.1. The total aperture is 400m and the baseline is 20m. We have used six Gaussian functions as basis functions. All of them have the

same amplitude - equal to one - and they have the same variance three by three. The constellation used here for the simulations is the same of the full constellation of the data set for the experimental results. We have simulated

(a) Gaussian basis functions   (b) Singular values trend
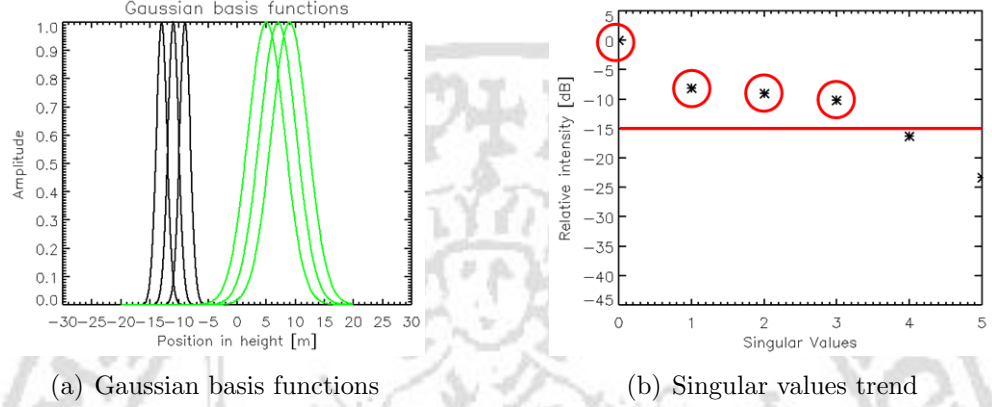
Figure 4.2: Simulated data using 21 tracks

a real distribution with two gaussian, one related to the ground response and the other one to model the canopy. The amplitude ratio is equal to 0.7, the distance between the maximum is equal to $18m$. The variance related to the ground is $25cm$ and for the canopy is $10m$. Using the TSVD we can notice the last two values have been ignored for the inversion (see Figure 4.2 (b)). The reconstruction (see Figure 4.3), represented in the figure with the red
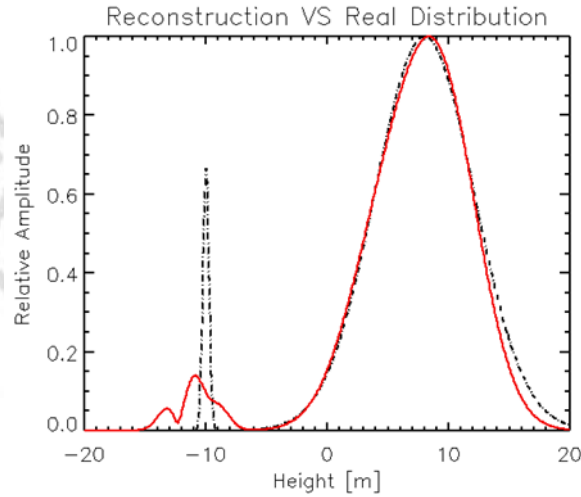
Figure 4.3: Reconstruction using SVD with 21 tracks

line, matches almost completely the real distribution for the canopy, while

we obtain some information about the position of the ground. In the following figure we can see the singular functions that represents the functions used by SVD to evaluate the weighting coefficients for the basis functions. Then, we have done a simulation with 8 tracks. Starting from a 8 regular
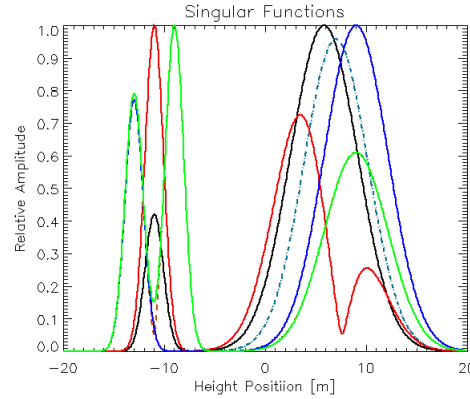
Figure 4.4: Singular functions for SVD inversion with 21 tracks

tracks constellation we have optimised the singular values trend obataining the "best" constellation that gives the "best" conditioning of the problem. Then, we have done a comparison between the reconstructions before and after the optimisation. Thanks to the optimisation, the singular values trend is
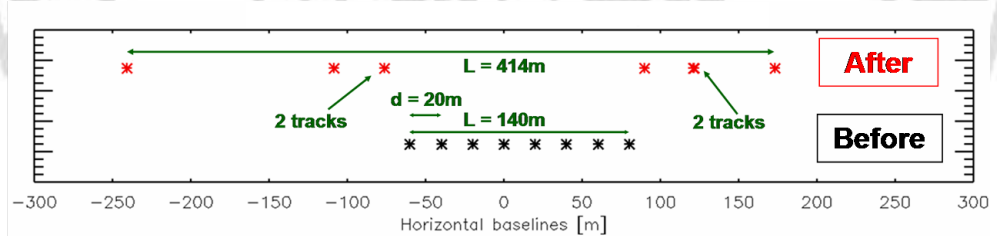
Figure 4.5: Constellation of 8 tracks before and after optimisation

now higher and it is possible to use two singular values more, collecting more information to retrieve the height profile (see Figure 4.6). Improvements can be noticed in the reconstruction with the optimised constellation (see Figure 4.7(a),(b)). Now we obtain more information about the ground and a more precise matching with the Gaussian related to the canopy. To test the robustness of the algorithm for the optimisation we ha done a simulation starting from a non-regular 8 tracks constellation and after the optimisation we have obtained the same constellation as before.

49
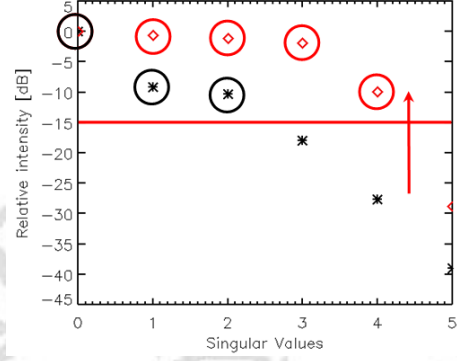
Figure 4.6: Singular values trend before optimisation (black stars) and after (red diamonds)
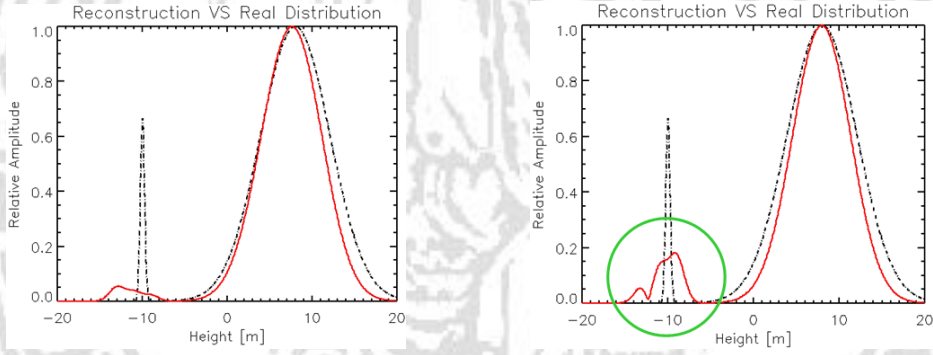
(a) Reconstruction before optimisation

(b) Reconstruction after optimisation

Figure 4.7: Simulated data using 8 tracks
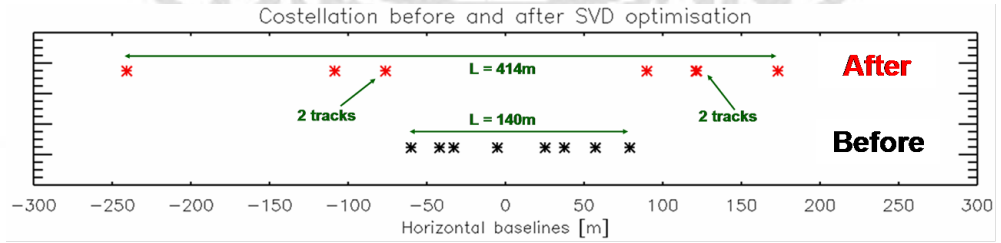
Figure 4.8: Constellation of 8 tracks before (non-regular) and after optimisation

4.1.2 Parametric inversion: simulated results

In the following subsection we will present results with simulated data using the parametric approach explained in the section 3.3.

The first results obtained are obtained using a conventional local minimisa-
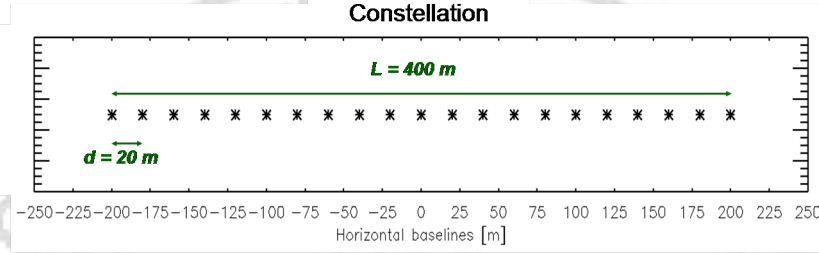
Figure 4.9: 21 tracks constellation

tion using 21 tracks, as we can see in the figure 4.9, depicting the constellation of 21 tracks. Using a local minimization we are not able to find the global minimum but for each simulation we obtain a different local minimum, as the figure 4.10 shows. We start from different starting points and we obtained different results corresponding to different local minimum. The black line represents the real distribution and the green one is the reconstruction. For
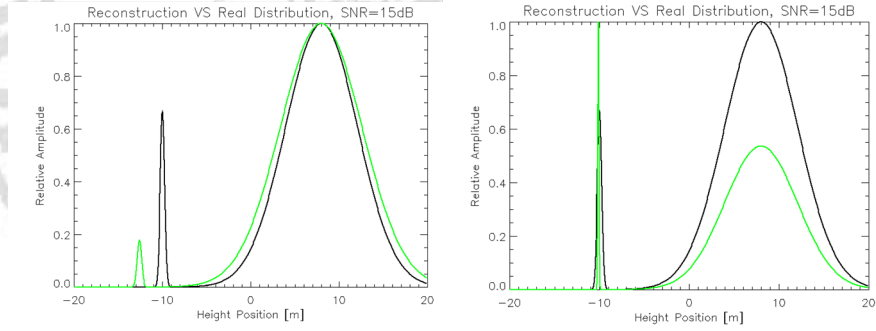
Figure 4.10: Simulated reconstructions using 21 tracks with local optimization

this reason we need a more efficient minimization method, such as the MLSL. Using this global optimisation algorithm we can notice an improvement in our reconstructions, both using 21 tracks and 8 tracks. Instead, from Figure 4.11 the reconstructions are very close to the real distribution, proving the correct solution of the MLSL algorithm.

51

(a) Reconstruction with 21 tracks   (b) Reconstruction with 8 tracks

Figure 4.11: Parametric reconstruction using MLSL

4.2 Experimental data analysis

Figure 4.12: Photo of Dornstetten forest

The data set has been acquired over the forest of Dornstetten (DE) in Semptember 2006. The airplane has flown several times building a 21 tracks constellation. The constellation has a total aperture of 400m and an average nominal baseline of 20m. The nominal height of flight is about 3760m. The experimental airborne SAR system was implemented by DLR and is called E-SAR. It is a Synthetic Aperture Radar system onboard of a DLR Dornier Do 228 aircraft (see Figure 4.13). In this case the sensor has operated in L-band (1.3 GHz) with horizontal polarization. The forest is caracterized by spruce trees with an average height of 16m. A cut along the azimuth of the forest has been analyzed, as we can see in the Figure 4.14. Due to the fact we have already acquired data from a certain constellation, we are limited to find the "best" 8 tracks constellation over the 21 already flown.

Figure 4.13: E-SAR Dornier Do 228-212 aircraft for remote sensing at DLR
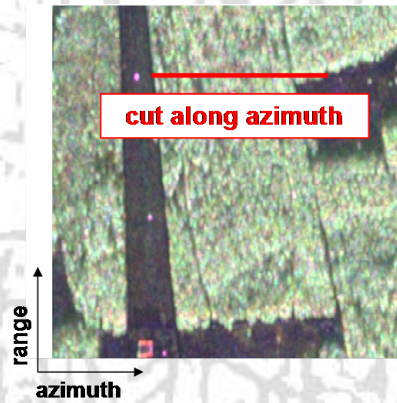
Figure 4.14: Polarimetric image of the Dornstetten forest. The red line represents the cut along which data set has been collected

4.3   Experimental results

In this section experimental results obtained from SVD inversion and from the parametric approach will be shown. We present firstly reconstructions using the full constellation of 8 tracks and then with the reduced system (8 tracks).

4.3.1 Full system reconstruction

The experimental result using 21 tracks has been obtained using SVD inversion. We have choosen a set of Gaussian basis functions with the same amplitude and the same variance three by three. For each processed azimuth
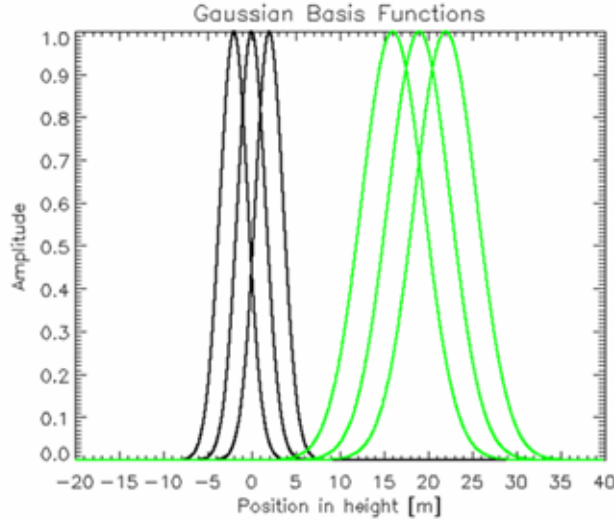
Figure 4.15: Gaussian basis functions used for experimental results

bin we obtain a reconstruction that is a linear combination of the basis functions. If we collect all the reconstructions we can make a tomogram. In this tomogram, the x-axis represents the azimuth and the y-axis is the height. The colours show the intensity of the density profile retrieved from the inversion. Comparing this result with the reconstruction using Fourier inversion with the same full constellation, we can notice many similarities about the ground information and the canopy. For example, where there is a little road in the forest in both reconstructions we can distinguish only the ground response, while the canopy is absent. In certain areas there is a dense vegetation and we can notice in both reconstructions a high backscattered signal related to the canopy and a low response for the ground. At the end of forest, there is a river and in both reconstruction we can observe that the backscattered signal is very low and random. We have to point out that Fourier reconstruction has used a polarimetric information and the color (red, blue and green) stands for three different scattering mechanisms (Pauli 1, Pauli 2, Pauli 3). Doing an average in azimuth of the reconstructions we obtain the following shape and we can see that the distance between two phase centers of ground and canopy is averagelly 16m.
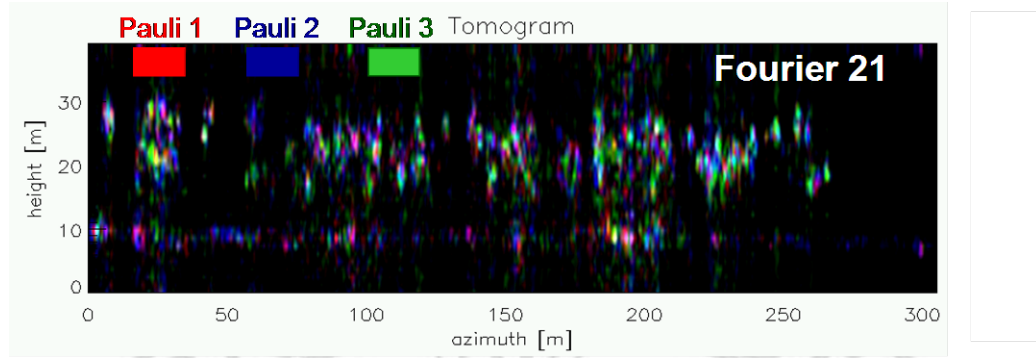
(a) Reconstruction with Fourier polarimetric
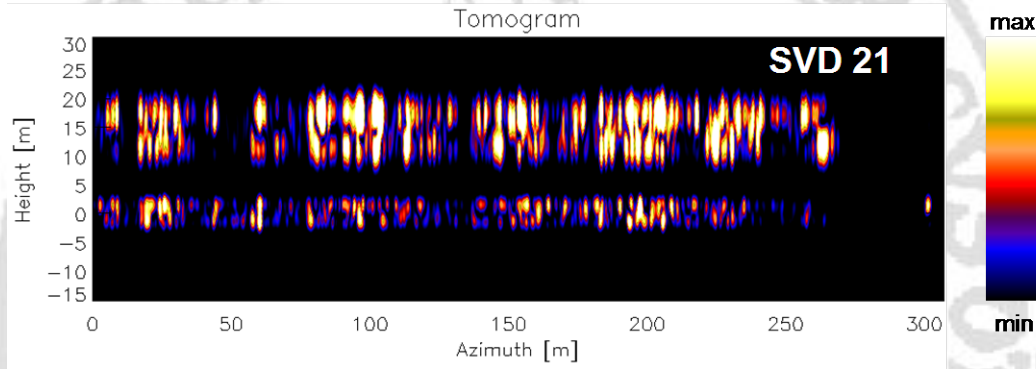
(b) Reconstruction with SVD inversion

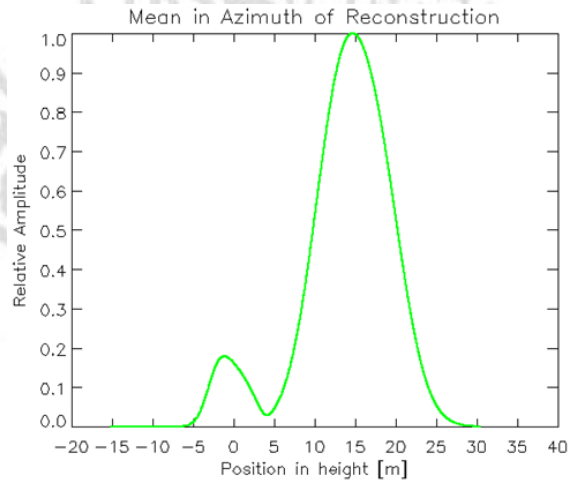Figure 4.16: Reconstructions with full constellation (21 tracks)

Figure 4.17: Mean in azimuth of reconstructions with 21 tracks

4.3.2   Reduced system reconstruction

In the case of real data the optimisation has worked choosing the 8 tracks, out of the 21 already flown, that give the best singular values trend. We have choosen the same set of basis functions used for the full constellation. As we can see from the Figure 4.19 we have an improvement of several orders of magnitude between the "best" constellation (red diamonds) and the "worst" one (black stars). Even if we have drastically reduced the number of tracks
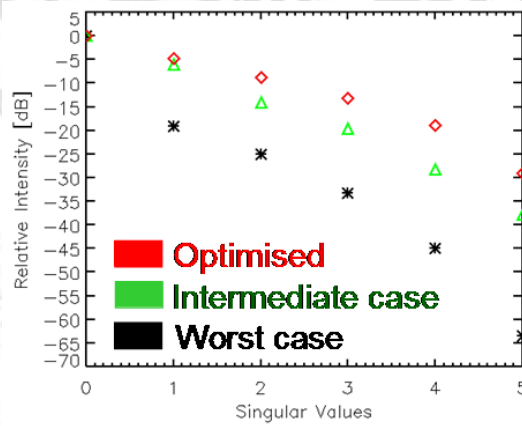
Figure 4.18: Singular values for different constellations

we still are able to retrieve informations in the height direction. Compared to the Fourier reconstruction using 21 tracks, the reconstruction with SVD using the "best" 8 tracks constellation has similarities and show information where the canopy is very dense, where there are no canopy contribution due to the presence of a street, and a low backscattered signal in correspondence to the presence of the river.
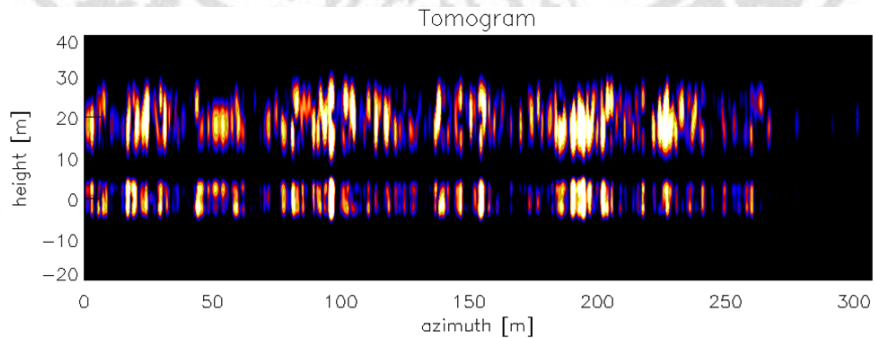

Figure 4.19: Reconstruction with the "best" 8 tracks constellation

The mean in azimuth of the reconstruction gives us a distance between the two phase centers of 17m. Doing several simulations changing the set of
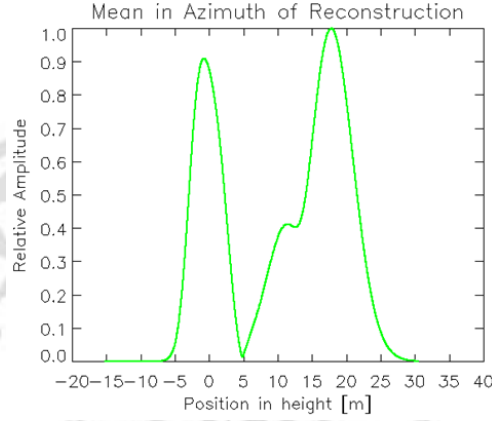

Figure 4.20: Mean in azimuth of reconstructions with "best" constellation

basis functions we have noticed that the reconstruction is basis dependent. This feature can lead to a bad reconstruction if the basis functions represent a very strong constraint and they don't match with the reality.
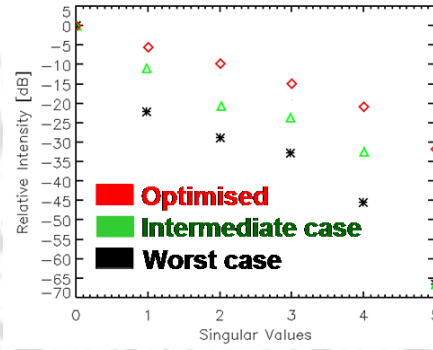

Figure 4.21: Singular values for different constellations in the case of bad basis functions
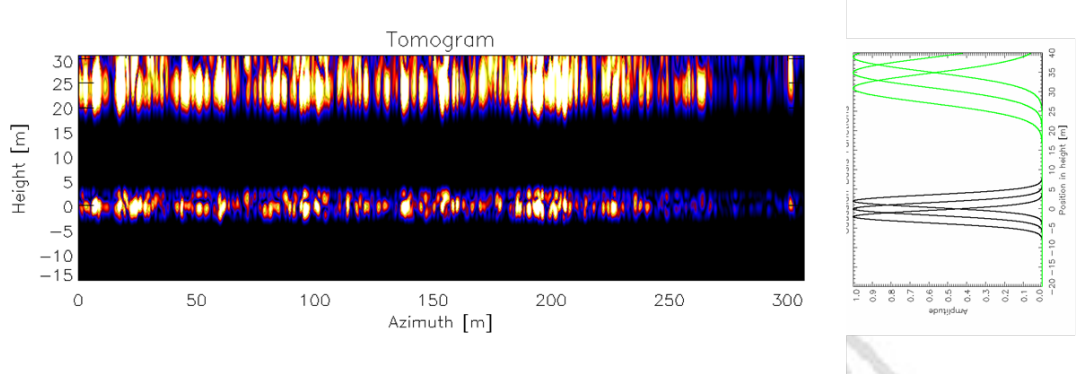
Figure 4.22: Reconstruction with the 8 tracks constellation using bad basis functions

For this reason we have tried to implement a solution to mitigate the dependece on the a priori information we have inserted into the model. We have defined 20 different sets of basis functions and we have found the "best" constellation in average for all these 20 sets of Gaussian functions.
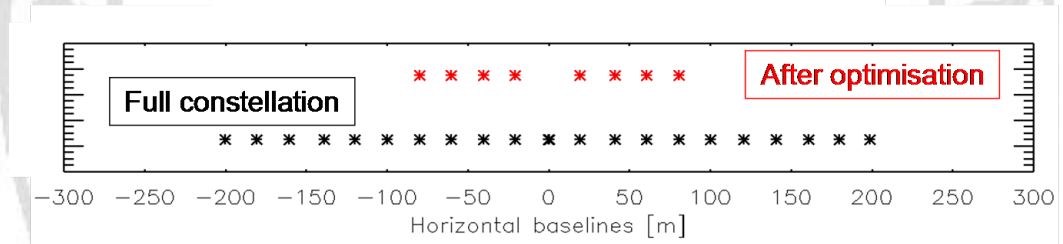

Figure 4.23: Constellation before and after optimisation with 20 sets of basis functions

Figure 4.23 represents the full constellation before the optimisation and the reduced system after the optimisation. The reconstruction shows also for this constellation similarities compared to the reconstruction with Fourier using the full system.

We can check also in this case that it is possible to retrieve informations where the canopy is much more dense and where is present the street and there is only the ground contribution. Also in this case, doing the mean
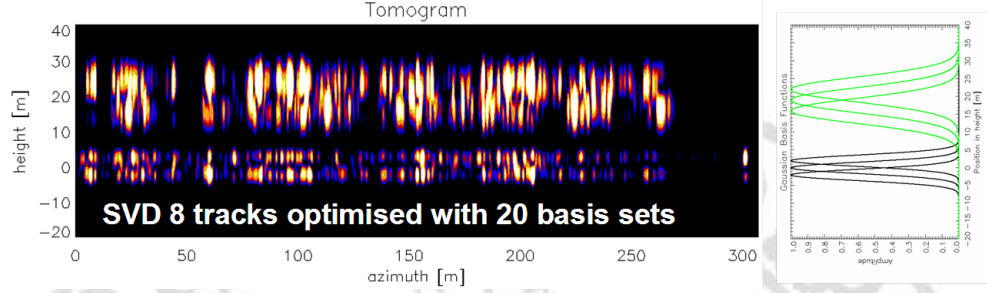

Figure 4.24: Reconstruction with the "best" 8 tracks constellation using 20 sets of basis functions

in azimuth of reconstructions we obtain a distance between the two phase centers - the maxima of the two gaussians - of 16m.
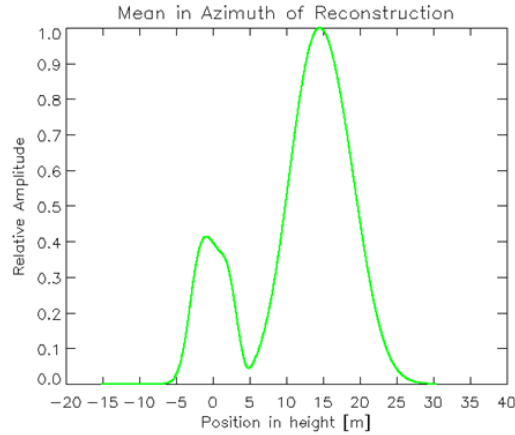

Figure 4.25: Mean in azimuth of reconstructions optimising with 20 sets of basis functions

The final step done in this work has been to combine the optimisation of constellation based on SVD with the parametric inversion. We have done a comparison between the reconstruction retrieved with a regular 8 tracks constellation and the reconstruction with the optimised constellation.

Using the parametric approach we can notice the reconstruction seems to be more stable in the case of the optimised constellation. Using the regular constellation, instead, the ground in some points oscillates. The paramteric method, moreover, should perform a better resolution compared with the normal SVD inversion. In fact, observing parametric reconstructions it is clear that the ground is more thinner showing a better resolution.
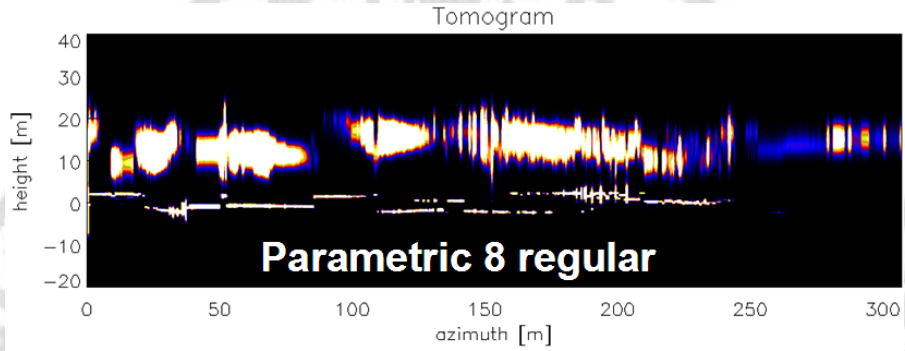
(a) Reconstruction with 8 regular tracks
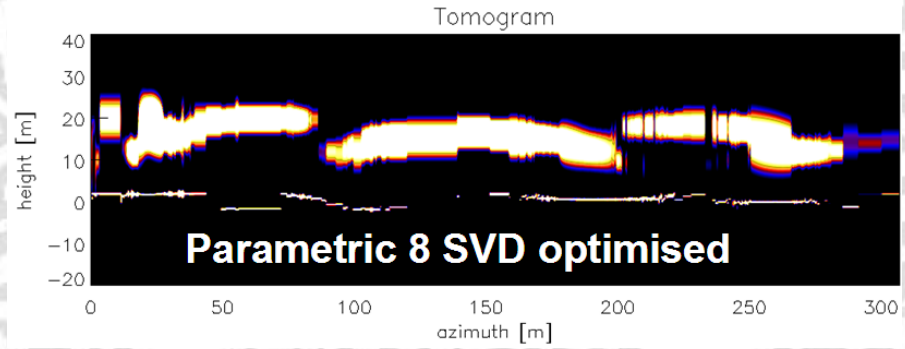
(b) Reconstruction with 8 optimised tracks

Figure 4.26: Parametric reconstruction with 8 tracks

Bibliography

[Bert 98]   Bertero, M. and Boccacci, P. "Introduction to Inverse Problems in Imaging". *Institute of Physics Publishing, 1998.*

[Capoz 06] A. Capozzoli and G. D'Elia "Global optimization and antennas synthesis and diagnosis, Part two: Applications to advanced reflector antennas synthesis and diagnosis techniques". *Progress In Electromagnetics Research*, pp. 233–261, 2006.

[Capoz 07] Capozzoli, A. and D'Elia, G. and Liseno, A. and Moreira, A. and Papathanassiou, KP "A novel optimization approach to forest height reconstruction from multi-baseline data". *IEEE International Geoscience and Remote Sensing Symposium, 2007. IGARSS 2007*, pp. 5037–5040, 2007.

[Clou 98]   Cloude, SR and Papathanassiou, KP "Polarimetric SAR interferometry". *IEEE Transactions on Geoscience and Remote Sensing*, Vol. 36, No. 5, pp. 1551–1565, 1998.

[Clou 03]   Cloude, SR and Papathanassiou, KP "Three-stage inversion process for polarimetric SAR interferometry". *IEEE Transactions on Geoscience and Remote Sensing*, Vol. 150, No. 3, pp. 125–134, 2003.

[Cumm 04] Cumming, I.G. and Wong, F.H. "Digital Signal Processing of Synthetic Aperture Radar Data: Algorithms and Implementation". *Artech House, 2004,*

[Forn 03]   Fornaro, G. and Serafino, F. and Soldovieri, F. "Three-dimensional focusing with multipass SAR data". *IEEE Transactions on Geoscience and Remote Sensing*, Vol. 41, No. 3, pp. 507–517, 2003.

[Loc 99]   Locatelli, M. and Schoen, F. "Random Linkage: a family of acceptance/rejection algorithms for global optimisation". *Mathematical Programming, Springer*, Vol. 85,pp. 379–396, 1999.

[Mette 02] T. Mette and KP. Papathanassiou. "Forest biomass estimation using polarimetric SAR interferometry". *2002 IEEE International Geoscience and Remote Sensing Symposium, 2002. IGARSS'02*, Vol. 2, 2002.

[Mette 02] T. Mette "Forest biomass estimation from polarimetric SAR interferometry". *PhD thesis, 2007 Universität Muenchen.*.

[Nakh 99]   Nakhkash, M. and Huang, Y. and Fang, MTC "Application of the multilevel single-linkage method toone-dimensional electromagnetic inverse scattering problem". *IEEE Transactions on Antennas and Propagation*, Vol. 47, No. 11, pp. 1658–1668, 1999.

[Nann 08]   Nannini, M. and Scheiber, R. and Moreira, A. "On the Minimum Number of Tracks for SAR Tomography". *IEEE Transactions on Geoscience and Remote Sensing Symposium, 2008. IGARSS 2008*, Vol. 2, 2008.

[Nann 09]   Nannini, M. and Scheiber, R. and Moreira, A. "Estimation of the Minimum Number of Tracks for SAR Tomography". *IEEE Transactions on Geoscience and Remote Sensing*, Vol. 47, No. 2, pp. 531–543, 2009.

[Olm 93]   Olmsted, C. "Alaska SAR Facility scientific SAR user's guide". *University of Alaska Fairbanks, Geophysical Institite. ASF-SD-003, 1993.*

[Prat 04]   Prats, P. and Reigber, A. and Mallorqui, JJ "Interpolation-free coregistration and phase-correction of airborne SAR interferograms". *Geoscience and Remote Sensing Letters, IEEE*, 2004.

[Reig 00]   Reigber, A. and Moreira, A. "First demonstration of airborne SAR tomography using multibaseline L-band data". *2002 IEEE Transactions on Geoscience and Remote Sensing, 2000.*, Vol. 38, No. 5, pp. 2142–2152,

[Reig 01]   Reigber, A. "Airborne Polarimetric SAR Tomography". *PhD thesis, 2001 Universität Stuttgart.*

[Rinnoo 87] Rinnooy Kan, A.H.G. and Timmer, G.T. "Stochastic global optimization methods part I: Clustering methods". *Mathematical Programming, Springer*, Vol. 39, No. 1, pp. 27–56, 1987.